Petroleum Science 23 (2026) 1261–1279

Contents lists available at ScienceDirect

Petroleum Science

journal homepage: www.keaipublishing.com/en/journals/petroleum-science

Original Paper

Mechanical, structural, and mineralogical changes of shale under acid-CO_2-rock interactions and their implications for CO_2 storage

Hang Zhou [a], Bo Wang [b,*], Fu-Jian Zhou [a]

[a] State Key Laboratory of Petroleum Resources and Engineering, China University of Petroleum (Beijing), Beijing, 102249, China
[b] China University of Petroleum-Beijing at Karamay, Karamay, 834000, Xinjiang, China

ARTICLE INFO

Article history:
Received 22 July 2025
Received in revised form
24 August 2025
Accepted 2 December 2025
Available online 8 December 2025

Edited by Min Li

Keywords:
CO_2-acid-rock interactions
Shale reservoir
Mineralogical alterations
Microstructure evolution
Nanomechanical properties
CO_2 storage

ABSTRACT

Elucidating the underlying chemo-mechanical coupling mechanisms of acid-supercritical carbon dioxide ($scCO_2$) reactions in shale reservoirs is essential for advancing the efficacy and safety of CO_2 geo-storage and enhanced oil recovery (EOR) techniques. Multi-scale experiments-including X-ray diffraction (XRD), scanning electron microscopy (SEM), nuclear magnetic resonance (NMR), atomic force microscopy (AFM), and nanoindentation-were used to characterize changes in mineralogy, pore structure, and mechanical properties under hydrochloric acid (HCl) pretreatment, followed by $scCO_2$ exposure. Results demonstrate that acid pretreatment acts as an efficient method to dissolve carbonate minerals, effectively boosting secondary porosity and $scCO_2$ accessibility. Subsequent exposure to $scCO_2$ further modifies the mineral composition and induces a marked enhancement in pore-fracture connectivity, as revealed by advanced imaging and topographical analysis. The synergistic effect of acid and $scCO_2$, validated by nanoindentation and NMR, leads to considerable mechanical softening and superior hydrocarbon displacement efficiency. These findings establish the synergy between acid and $scCO_2$ in dynamically reshaping the shale pore-fracture system, thereby simultaneously enhancing hydrocarbon recovery and long-term CO_2 storage. This integrated approach offers a novel paradigm for optimizing reservoir stimulation within carbon capture, utilization, and storage CCUS frameworks.

1. Introduction

Energy demands are increasing with a growing global population and ongoing economic development. The growing imperatives of environmental protection and the transition to a low-carbon economy have established CCUS as a critical strategy for mitigating greenhouse gas emissions (Muhsin, 2024; Saló-Salgado et al., 2024). Deep geological formations have been extensively studied and identified as promising reservoirs for the long-term injection and storage of CO_2. Among the available options, they are widely regarded as one of the most viable solutions for mitigating atmospheric CO_2 emissions (Chen and Gu, 2017; Zhao et al., 2025). Extensive research efforts on geological CO_2 storage have predominantly centered on conventional formations, such as deep saline aquifers (Ali, 2023). The advent of large-scale shale reservoir production has subsequently stimulated interest in utilizing these formations for CO_2 storage (de Silva et al., 2012). CO_2 injection into shale reservoirs offers the dual benefit of improving reservoir properties and displacing in-situ hydrocarbons, representing two complementary mechanisms for enhanced recovery (Alfayyadh, 2024; Guo et al., 2024; Zhang et al., 2025). Despite growing scholarly attention on CO_2 storage in shale reservoirs, a critical research gap remains in the strategic optimization of reservoir conditions to simultaneously enable efficient CO_2 injection, hydrocarbon displacement, and maximized storage performance.

$ScCO_2$ injection into shale reservoirs is known to degrade its mechanical properties, resulting in a pronounced diminution of tensile strength, triaxial compressive strength, and elastic modulus (Zhou et al., 2021; Alsultan et al., 2023; Li et al., 2025). This weakening primarily stems from $scCO_2$-induced alterations to the shale particle skeleton and pore structure. Specifically, the dissolution and mobilization of minerals by $scCO_2$ modify the pore morphology, leading to a decline in the proportion of micro- and mesopores while concurrently increasing overall porosity and connectivity (He et al., 2023; L. Zhang et al., 2023). At a larger

* Corresponding author.
E-mail address: wangbo@cupk.edu.cn (B. Wang).
Peer review under the responsibility of China University of Petroleum (Beijing).

https://doi.org/10.1016/j.petsci.2025.12.002

structural scale, $scCO_2$ also alters the bedding structure, primarily by compromising the mechanical integrity of the bedding planes (Bai et al., 2021). The influence of $scCO_2$ on shale mechanics is closely linked to mineral composition changes (Tian et al., 2023). Experimental results demonstrate that $scCO_2$-water soaking dissolves portions of the clay and carbonate minerals, thereby enlarging the pore size and increasing the total pore volume of the shale matrix (Yang et al., 2023). This mineral dissolution and pore evolution weaken the rock's structure and lower mechanical properties. Furthermore, pressure and temperature strongly influence $scCO_2$'s impact. Increased CO_2 pressure makes shale initially expand, then contract. In contrast, rising temperature gradually lessens the maximum expansion (Lu et al., 2016). Under an elevated thermal regime, the shale matrix evolves through a process of pore coarsening, evidenced by a decreasing specific surface area, a transition from micro- and mesopores to macropores, and a higher resultant CO_2 pore concentration (Zhou et al., 2025a).

The reaction of acid with shale minerals generates dissolution pores, thereby enhancing reservoir porosity and permeability. This chemical alteration softens the shale matrix, reducing its stiffness and strength, which in turn governs the subsequent mechanical response-including deformation behavior and fracture propagation. Studies indicate that acid pretreatment effectively lowers the fracture initiation pressure. Furthermore, in naturally fractured zones, acid-rock reactions intensify, leading to more complex fracture networks. Soaking experiments reveal distinct microfracture mechanisms: (a) in clay-rich shale, microfractures are primarily induced by ion expansion and migration; whereas (b) in carbonate-rich shale, they result from interfacial ion precipitation effects (Sheng et al., 2021). Nitrogen adsorption experiments confirm that acid treatment decreases the fractal dimension of shale surfaces and increases that of micropores. This shows nanopore walls are smoother after acid treatment. In shales high in carbonate, the nanopore size distribution becomes more uneven, and structural anisotropy weakens (Xu et al., 2023a). For Wujiaping Formation Shale, 15% hydrochloric acid dissolves reactive minerals, expands pores and fractures, and lowers triaxial compressive strength, elastic modulus, and Poisson's ratio (Zhang et al., 2024). After the acid reaction, the wettability of shale changes from hydrophilic to neutral, altering reservoir fluid migration (Cheng et al., 2024).

Injecting CO_2 into shale oil reservoirs can enhance oil recovery by reducing viscosity and displacing pore fluids (Cui et al., 2011). Nuclear magnetic resonance experiments show that CO_2 foam flooding boosts recovery in fractured and non-fractured cores by 47.8% and 39.1%, respectively (Li et al., 2020). Under miscible conditions, a linear relationship exists between CO_2 injection pressure and recovery rate in small shale pores. As pressure increases, the lower limit of mobilized pores drops (Huang et al., 2022). Additional research shows that miscible flooding works well in reservoirs with permeability over 10 mD. When pressure exceeds the miscible point, the recovery rate can surpass 85%. However, high-pressure stimulation becomes less effective at that point. Immiscible flooding is more suitable for low-viscosity reservoirs (Wang et al., 2023). Molecular dynamics simulations show CO_2 displacement efficiency in hydrophilic systems is 98.77%, much higher than 41.90% in mixed-wettability systems. This is mainly due to strong interactions between CO_2 and methyl or hydroxyl groups on the rock surface (Xu et al., 2024).

Geological CO_2 storage is a key emission reduction method. It is applied in oil and gas fields, deep coal seams, and saline aquifers. Oil and gas fields offer dual benefits: enhanced recovery and storage. Studies show the CO_2 adsorption capacity follows this order: organic matter > montmorillonite > illite > kaolinite > quartz. A 10 Å increase in pore size causes a 38% drop in adsorption capacity (Wu et al., 2024). In shale gas reservoirs, simulations show the CO_2 adsorption phase capture ratio can reach 30%–55%. Natural gas recovery can rise 8%–16% at the same time. This shows that adsorption storage is superior to traditional dissolution methods (Mohagheghian et al., 2019). Further molecular dynamics and CMG simulations confirm the strong adsorption of kerogen, enhancing storage stability. The dimethyl ether cosolvent leads to the highest storage rate (98.3%). The ethyl acetate system offers the best storage stability (Y. Zhang et al., 2023). Sensitivity analysis reveals that raising injection pressure from 5.5 to 8.5 MPa boosts storage by a factor of 6.8. Reservoir parameters are more sensitive at high injection pressures (Wang et al., 2023). Reservoirs with low water saturation (less than 20%) and low porosity (0.1) achieve maximum CO_2 storage.

This study proposes and mechanistically validates a novel acid-$scCO_2$ coupling approach to engineer shale reservoirs for improved CO_2 storage and enhanced recovery. Utilizing a coupled experimental methodology, we unravel the dynamic evolution of shale properties under chemical-mechanical stimulation, with NMR-derived pore structure parameters directly correlated to storage efficiency. These findings offer fundamental theoretical support for advancing CO_2-EOR synergistic storage technologies.

2. Materials

The experimental core was collected from a shale reservoir (Fig. 1). The reservoir has an average porosity of 3.1%, an average permeability of 0.014 mD, and an average oil saturation of 55%. Clay mineral intergranular pores and dolomite dissolution pores are the primary storage spaces in the shale. Microfractures and laminae are also well developed (Fig. 2). The vertical stress is 78.24 MPa, the maximum horizontal principal stress is 73.39 MPa, and the minimum horizontal principal stress is 68.3 MPa. The tensile strength is 247.74 MPa, Young's modulus is 64.2 GPa, and Poisson's ratio is 0.29.

The microstructural characteristics of the shale as observed by SEM, are as follows (Fig. 2):

a. **Clay mineral intergranular pores**: These pores are located between clay mineral particles and serve as primary pathways for fluid flow in shale reservoirs. Variations in their morphology and size can significantly influence the reservoir's permeability and porosity.
b. **Dolomite dissolution pores**: These pores form because of dolomite dissolution by acidic fluids or natural geological

Fig. 1. Shale samples.

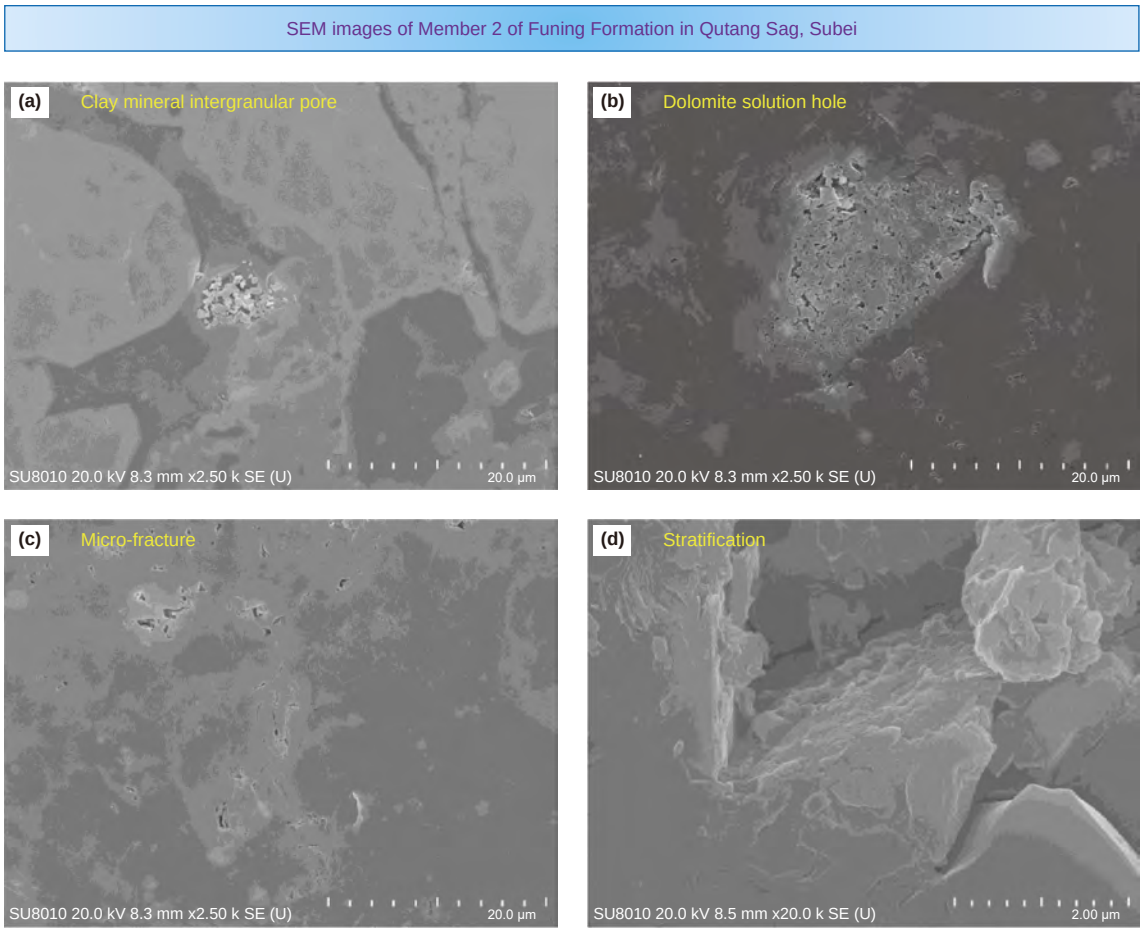

Fig. 2. Scanning electron microscopy (SEM) images of shale microstructure: (**a**) Clay mineral intergranular pores; (**b**) Dolomite dissolution pores; (**c**) Microfractures; (**d**) Bedding structure.

processes. The presence of such pores enhances both porosity and permeability, thereby facilitating the migration of fluids.

c. **Microfractures**: Microfractures, typically generated by geological stress or changes in fluid pressure, substantially improve permeability by providing additional flow channels.
d. **Stratification**: SEM images reveal pronounced stratification within the shale, likely due to fluctuations in sedimentation rate and depositional environment. Stratification contributes to reservoir anisotropy, resulting in directional differences in physical properties.

These microstructural attributes fundamentally underpin the porosity, permeability, and ultimately dictate the fluid flow behavior within the shale reservoir.

Multiple 1-inch standard cores were drilled from a single full-diameter shale core. For clarity, samples exposed to hydrochloric acid followed by supercritical CO_2 were labeled as HSC-1 to HSC-8 (HSC for HCl + $scCO_2$), while those exposed only to supercritical CO_2 were designated SC-1 to SC-8 (SC for $scCO_2$). This was done for soaking experiments to maintain consistent mineralogical and mechanical properties across samples. This sampling approach ensured both the representativeness and repeatability of the experiments. Two soaking environments were established: 15% hydrochloric acid (HCl) and $scCO_2$. The 15% hydrochloric acid soaking group involved two steps. First, the cores, after being saturated with crude oil, were placed in 15% hydrochloric acid for 3 h. Then, they continued soaking in supercritical carbon dioxide for different durations. Samples in each environment were soaked at 90 °C. The $scCO_2$ soaking experiments were conducted at a pressure of 30 MPa. Soaking durations were 2, 4, 6, 15, 30, 45, and 60 days, respectively, to assess the effects of different soaking times on the shale samples (Fig. 3).

The soaking times were set at 2, 4, 6, 15, 30, 45, and 60 days. These intervals capture both short- and long-term interactions between shale and the acid-$scCO_2$ system. The short time points of 2–6 days target early-stage dissolution dynamics of carbonate minerals. The 15-30-day periods allow assessment of progressive changes in pore networks. Longer durations, 45–60 days, simulate extended exposure typical of subsurface storage. This range of intervals ensures comprehensive temporal resolution for evaluating coupled chemical-mechanical effects.

3. Methods

3.1. Mineralogical testing

A series of measurement methods was used to study changes in mineral composition, oil content, pore and fracture structure, and mechanical properties of shale under acid etching and $scCO_2$. XRD was used to measure quartz, clay, and carbonates in the shale to analyze mineral makeup. For sample prep, shale was ground to under 50 μm to avoid mineral orientation. The powder was pressed into a thin pellet or loaded into the sample holder by back-

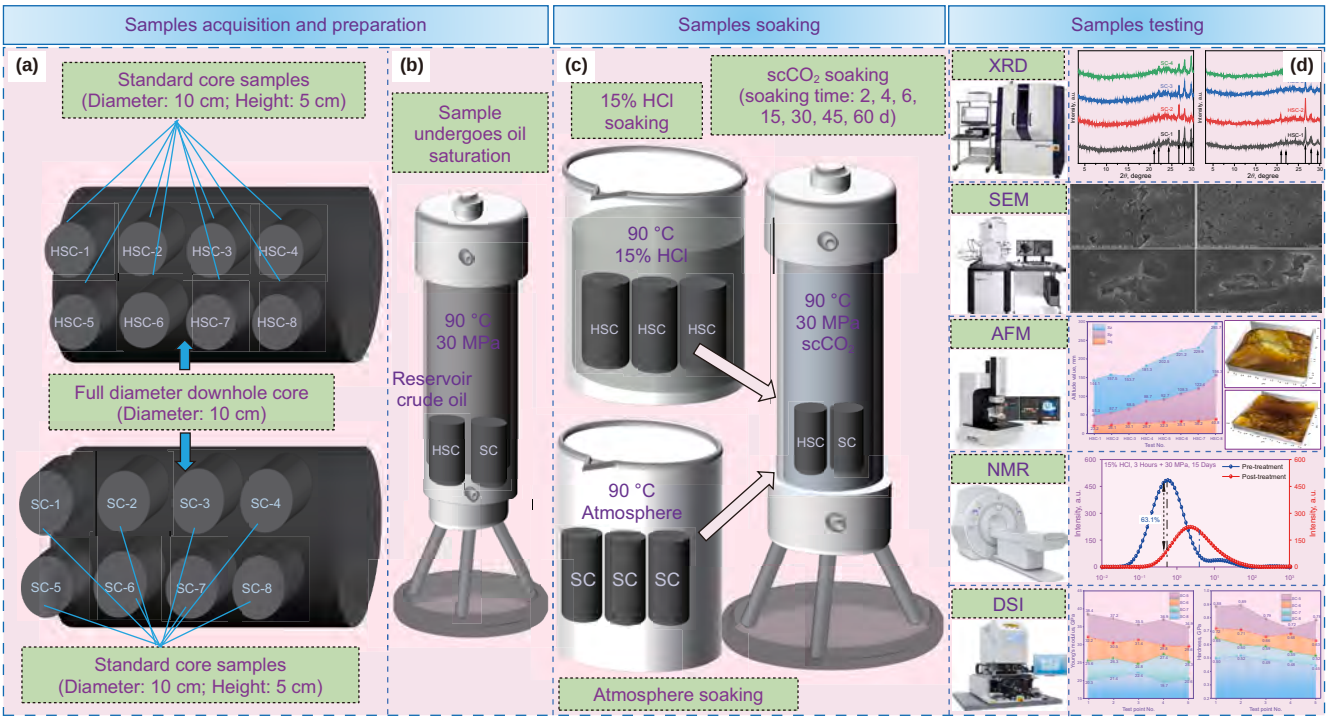

Fig. 3. Soaking experiment process and testing methods.

loading. Scanning parameters were set and data collected with a 3.5°–30° range, step size 0.02°, and speed 3° per minute. Finally, semi-quantitative mineral analysis was done using Jade or other tools like the Rietveld method or the reference intensity ratio method.

3.2. Structural testing

Field-emission SEM examined the microstructure, morphology, and pore structure of samples. The acceleration voltage (5–20 kV) and working distance (5–15 mm) were adjusted for resolution, using both secondary (SE) and backscattered electron (BSE) detectors. The resolution ranged from 1 to 5 nm in high-vacuum mode ($\leq 10^{-3}$ Pa). Shale samples, cut into 5 × 5 mm thin slices, had surfaces polished or argon ion milled to reduce mechanical damage. To minimize charging, a 5 nm conductive gold or carbon film coating was applied. Low-magnification imaging located regions of interest, such as organic matter bands or fractures, while higher magnifications (10–100 k) visualized nanopore structures. The distribution of mineral components was then analyzed by correlating BSE images and EDS mapping. Subsequently, AFM characterized nanoscale roughness and topography after acid and $scCO_2$ treatment. Measurements were made using a Bruker Dimension Icon AFM in tapping mode with silicon cantilevers. Scan sizes ranged from 1 × 1 μm^2 to 10 × 10 μm^2 at 512 × 512-pixel resolution. At least three different regions per sample were scanned for representativeness. Finally, RMS roughness and peak-to-valley height were extracted for quantitative comparison.

3.3. Nanomechanical testing

Nanoindentation testing was conducted to evaluate the micromechanical properties (hardness and elastic modulus) and heterogeneity of shale. Shale samples were first sectioned into flat blocks (approximately 1 cm^3) using a precision saw. The sample surfaces were then polished in sequential steps. First, they were ground with progressively finer abrasives. Next, they underwent final polishing using either ion polishing or precision grinding to achieve a surface roughness of less than 50 nm. Target test areas were identified using an optical microscope or SEM. Care was taken to avoid pores and fractures. A small preload was applied to confirm sample surface flatness before indents. The maximum load applied ranged from 1 to 50 mN and was adjusted according to shale hardness. A Berkovich diamond indenter with an equivalent half-angle of 65.3° was used. The loading rate ranged from 0.1 to 1 mN/s, with a holding time of 5–10 s to minimize creep effects. Displacement resolution was less than 0.1 nm. The loading, holding, and unloading procedures were performed, and load-displacement curves were recorded. At least 20 points were tested per sample to statistically analyze the distribution of mechanical properties. Hardness (H) and Young's modulus (E) were calculated using the Oliver-Pharr method, which relates applied load and indentation depth.

3.4. NMR testing

NMR testing uses magnetic fields and radio waves to examine materials at the atomic level. In this study, NMR was employed to characterize the pore structure and fluid distribution in shale. The instrument operated at a magnetic field strength of 0.5–3 T. Resonance frequencies ranged from 20 to 300 MHz. The Carr-Purcell-Meiboom-Gill (CPMG) pulse sequence was used for T_2 relaxation. The saturation recovery sequence was used for T_1 relaxation. Key experimental parameters included an echo time set to 0.1–1 ms. The waiting time exceeded 3 × T_1. The temperature was maintained between 25 and 80 °C to simulate formation conditions. For sample preparation, shale was cored into 2.5 cm diameter cylinders. The samples were washed and dried to constant weight. They were then evacuated and saturated with either simulated formation water or krypton gas to analyze micropores.

After saturation, samples were placed in the NMR probe. CPMG sequence parameters were set for at least 1000 echoes. The T_2 distribution curve, reflecting pore sizes, was then recorded. An inversion algorithm was applied to convert relaxation times to pore size distributions. Finally, movable and bound fluids were distinguished using centrifugation or freeze-thaw methods.

4. Results

4.1. Mineralogical alterations

XRD analyses were conducted on samples after acid and $scCO_2$ soaking to determine changes in shale mineral composition during acid-rock reactions and CO_2 storage. The primary minerals analyzed included quartz, plagioclase, calcite, pyrite, anhydrite, dolomite, and clay minerals. A comparative summary of the net mineralogical changes in the cores after different soaking times is presented in Table 1.

The results show a clear trend in mineral changes in shale after exposure to $scCO_2$ and acid soaking. After $scCO_2$ soaking, quartz, calcite, and dolomite content decreased, while plagioclase and clay minerals increased. Quartz and calcite steadily decreased over time, with the former dropping significantly, while plagioclase and clay minerals increased in response to the $scCO_2$ treatment (Fig. 4). Similarly, acid soaking caused a decline in quartz and calcite, with an increase in plagioclase and clay minerals, mirroring the trends seen with $scCO_2$ exposure. Overall, both treatments led to a notable decrease in carbonate minerals (calcite and dolomite) and quartz, while promoting the growth of plagioclase and clay minerals (Fig. 5). This shift is largely driven by the dissolution of carbonate minerals in acidic conditions and the alteration of silicates in CO_2-rich environments, highlighting the processes influencing shale during CO_2 storage and acid-rock interactions. The observed mineral changes are primarily attributed to acid-rock interactions and CO_2 storage processes. These reactions are essential for understanding the long-term behavior of shale reservoirs during CO_2 storage and acid-rock interactions.

The evolution of mineral contents during $scCO_2$ soaking (up to 60 d) revealed significant changes. Quartz, calcite, and dolomite showed a consistent decline in content, indicating dissolution under acidic conditions generated by $scCO_2$. In contrast, plagioclase and clay minerals increased, likely due to secondary mineral formation or relative enrichment as carbonates dissolved. These trends indicate that $scCO_2$ primarily dissolves carbonates and quartz, while promoting relative or absolute increases in aluminosilicate minerals. Cores pre-treated with acid showed similar but more pronounced trends during subsequent $scCO_2$ exposure. Acid treatment accelerated the dissolution of reactive minerals, further amplifying the effects observed with $scCO_2$ alone. The acid pre-treatment significantly enhanced mineral reactivity, particularly for quartz and dolomite. A comparative summary of net mineralogical changes is presented in Table 1 highlighting the impact of both $scCO_2$ and acid + $scCO_2$ treatments. These results provide critical insights into mineral dissolution and transformation mechanisms during CO_2 storage and acid stimulation in shale formations.

Table 1
Net mineralogical changes after 60 days of treatment.

Mineral	After $scCO_2$ soaking, %	After acid + $scCO_2$ soaking, %
Quartz	−69.1	−78.6
Calcite	−64.6	−69.0
Dolomite	−39.5	−44.6
Plagioclase	+46.6	+18.8
Clay minerals	+147.8	+121.7

Notes: "+" indicates an increase, and "−" indicates a decrease.

4.2. Surface and structural alterations

Upon entering the rock, $scCO_2$ fills the pores and fractures, reacting with specific minerals. Additionally, $scCO_2$ extracts certain components from crude oil, thereby altering its physical and chemical properties. As a super solvent, $scCO_2$ also removes fillings from intergranular surfaces, natural microfractures, and bedding planes. These physical and chemical interactions result in changes to the pore structure, fracture network, and surface morphology of the rock. Field-emission SEM was employed to observe microstructural changes in the core after acid and $scCO_2$ soaking to elucidate these processes.

In contrast, AFM was used to examine changes in surface morphology. AFM is an advanced microscopic technique that detects surface features based on interatomic forces, such as van der Waals forces. It can directly obtain atomic-resolution images without sample preprocessing, achieving nanoscale precision. The resulting photos are real-space height maps, with grayscale indicating height.

SEM images of the core surfaces after various durations of $scCO_2$ soaking are shown in Fig. 6. The SC-1 sample displays a few small pores and natural microfractures, most of which remain closed. After 2 days of soaking, some microfractures begin to open, indicating the onset of $scCO_2$-induced dissolution. After 4 days, small pores gradually enlarge, suggesting ongoing dissolution. After 6 days, $scCO_2$ begins to etch minerals, forming larger pores. By 15 days, locally etched pores and fractures appear, indicating an intermediate stage of pore evolution. At 30 days, pores generated by mineral dissolution begin to connect with activated microfractures, enhancing the connectivity of the pore network. After 45 days, these pores further enlarge, and additional microfractures are activated. After 60 days, quartz, calcite, and dolomite have fully reacted with $scCO_2$, and numerous microfractures are activated, resulting in an irregular and complex fracture network. This marks the final stage of pore evolution, characterized by substantially enhanced network connectivity, and improves $scCO_2$ storage and hydrocarbon recovery. Overall, as $scCO_2$ soaking time increases, microfractures are progressively activated, and pore sizes increase. Minerals such as quartz, calcite, and dolomite are etched by $scCO_2$, forming matrix pores and fractures that ultimately create a fractured zone. Some dislodged minerals may also block pore throats. In addition to penetrating existing pores and fractures, $scCO_2$ creates new structures by dissolving minerals, thereby improving overall connectivity.

The SEM results of core surfaces after acid treatment and various durations of $scCO_2$ soaking presents in Fig. 7. In the HSC-1 sample, some carbonate minerals reacted with acid to form etched pores, while the fillings within microfractures were dissolved. After 2 days of $scCO_2$ soaking, $scCO_2$ reacted with water that had infiltrated during acid treatment, resulting in the crystallization of certain inorganic salts due to oversaturation. After 4 days of soaking, $scCO_2$ began etching minerals within the core, creating pores and fractures, with detached minerals observed on the core surface. After 6 days, mineral alteration and dissolution by $scCO_2$ became more pronounced, forming numerous new pore and fracture structures. After 15 days, minerals such as quartz, calcite, and dolomite either fully reacted with $scCO_2$ or detached, forming an etched zone. The framework of this zone consisted of minerals in the shale that did not react with acid or $scCO_2$, such as pyrite. After 30 days, the etched zone gradually expanded outward, further increasing the available space for $scCO_2$ storage. After 45 days, under the scouring effect of $scCO_2$ flow, undissolved minerals

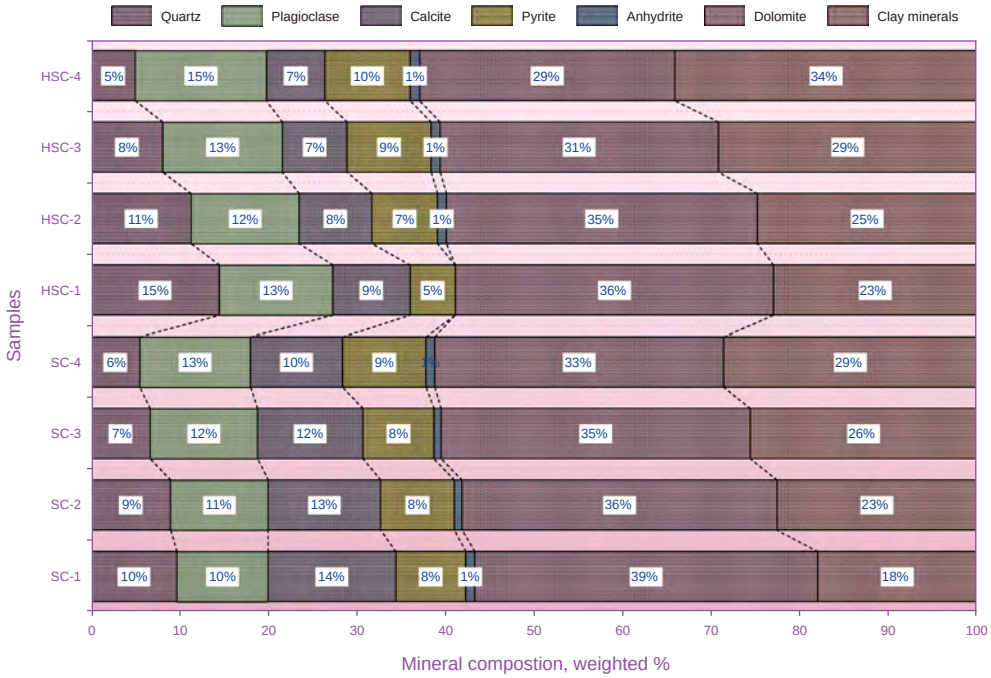

Fig. 4. Mineral contents in cores with different $scCO_2$ soaking times.

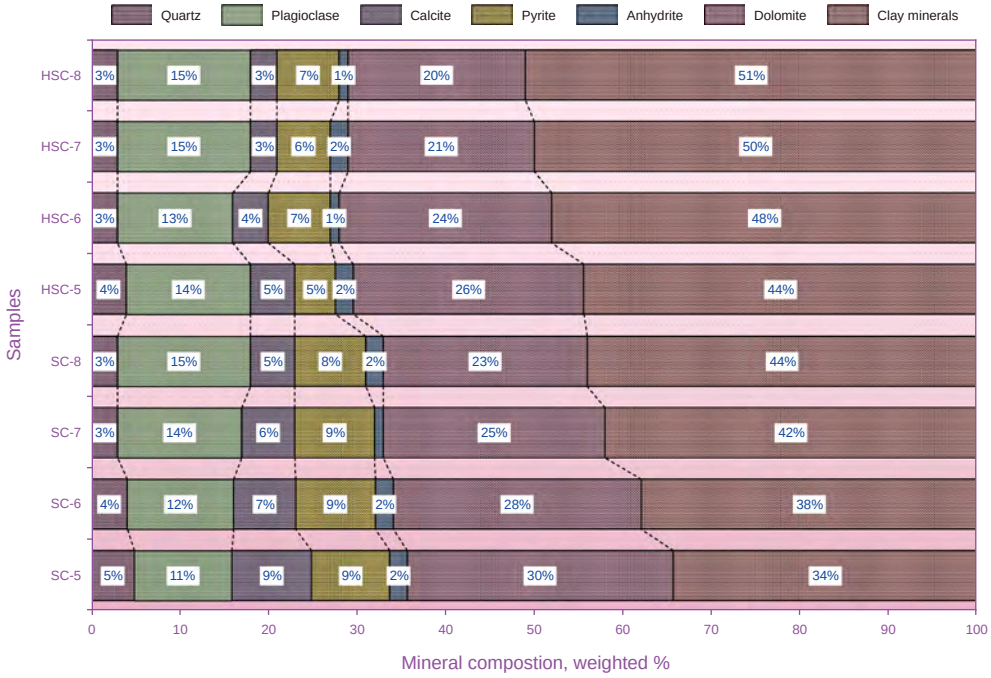

Fig. 5. Mineral contents in cores with different $scCO_2$ soaking times after acid treatment.

detached from the rock wall, forming large pore-fracture structures, with precipitates scattered on the pore surfaces. After 60 days, $scCO_2$ further etched the pore-fracture structures, and the rock wall became smooth due to continuous $scCO_2$ scouring, accompanied by significant dissolution and detachment of large-grained minerals. Overall, after acid treatment, carbonate minerals in the core were etched, and microfractures were activated, leading to the formation of new pore and fracture structures that provided effective flow paths for subsequent $scCO_2$ invasion (Thompson et al., 2013; Loring et al., 2014; Sanguinito et al., 2018). $scCO_2$ then migrated along these flow paths, gradually etching the surrounding rock to form an etched zone. This zone exhibited high porosity and permeability, further increasing the available volume for $scCO_2$ storage.

Swelling-induced constriction of shale pores and fractures occurs due to $scCO_2$ adsorption, primarily associated with mineral dissolution. Furthermore, the distinctive physicochemical properties of $scCO_2$, notably its high diffusivity and low viscosity,

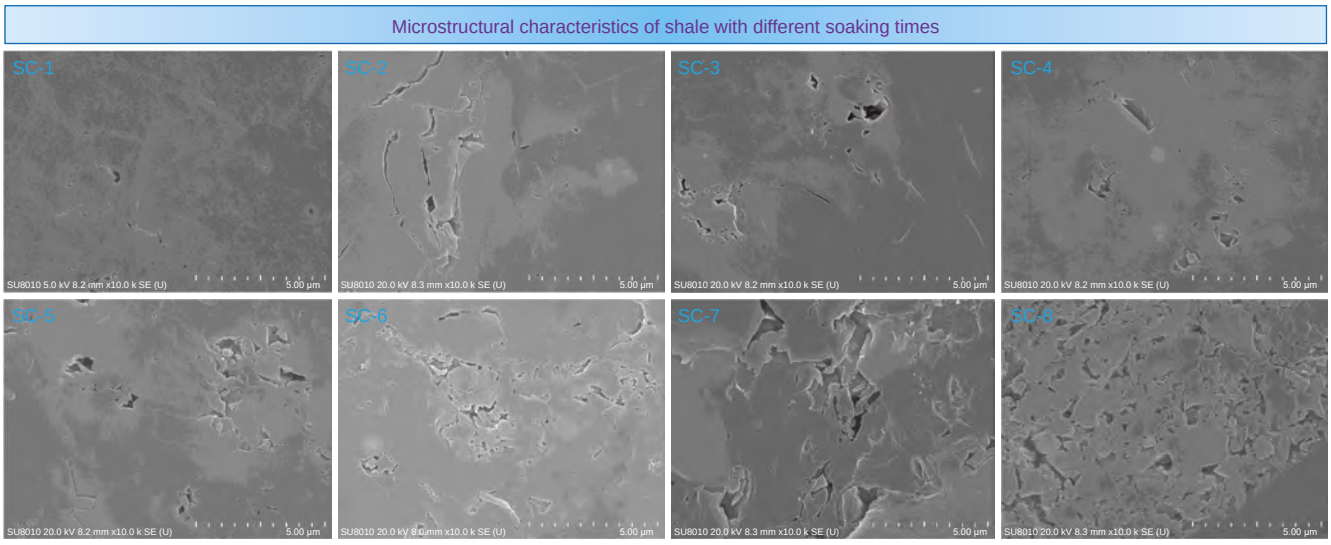

Fig. 6. Microstructural characteristics of shale under different $scCO_2$ soaking times.

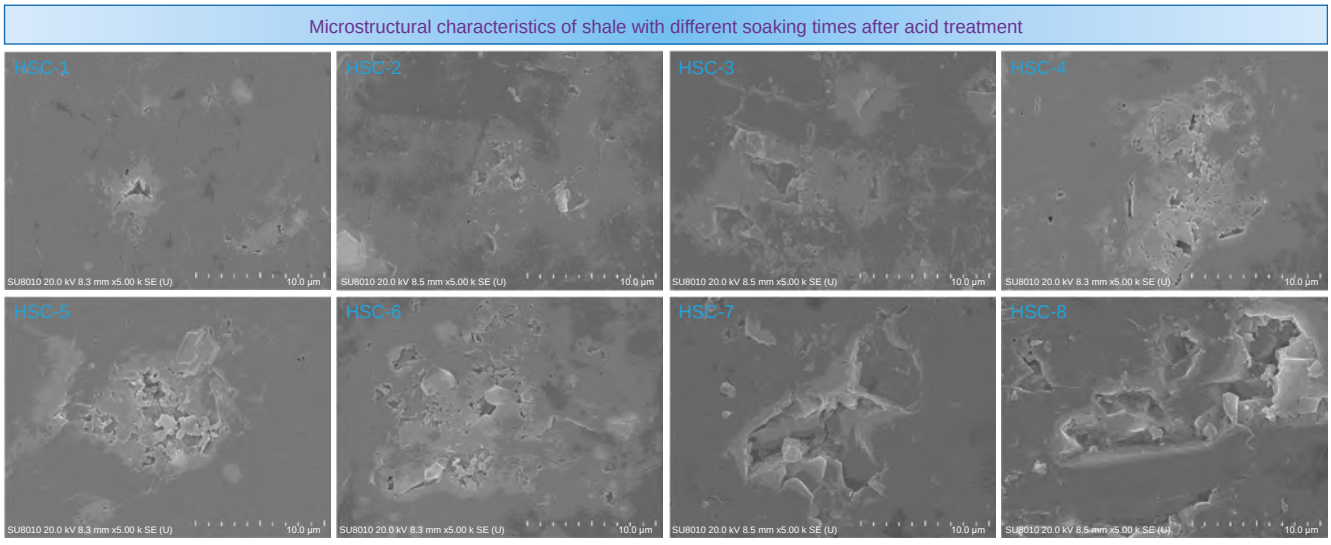

Fig. 7. Microstructural characteristics of shale with different $scCO_2$ soaking times after acid treatment.

empower it to act as a super-solvent, facilitating the extraction of non-polar hydrocarbons from the shale matrix (Jarboe et al., 2015; Jiang et al., 2016). AFM height images directly reveal the surface morphology and deformation characteristics of minerals. AFM results for shale surfaces after acid treatment and various durations of $scCO_2$ soaking are shown in Fig. 8. $ScCO_2$ soaking induces the formation of characteristic etched striations on the shale surface. These features are the result of $scCO_2$ scouring and progressively dissolving mineral components, thereby generating visible reaction pathways. The number of etched stripes reaches a maximum after 6 days of soaking. As the $scCO_2$ soaking duration increases, significant precipitation gradually forms on the shale surface. During acid treatment, the corrosion of certain minerals leads to the formation of numerous uneven points on the shale surface, identified as barite and salt precipitates (Sanguinito et al., 2020). Compared with resistant minerals such as apatite, carbonate minerals are more susceptible to barite precipitation in corroded regions. After $scCO_2$ soaking, additional precipitates appear on the shale surface. As $scCO_2$ soaking continues, the mineral irregularities on the acid-corroded shale surface are gradually removed, resulting in a step-like structural morphology. Barite precipitation predominantly occurs in altered carbonate areas rather than on resistant minerals such as apatite.

Combined SEM/AFM analysis reveals a coordinated pore-scale evolution: mineral dissolution simultaneously widens microfractures (SEM) and generates nanoscale surface roughness (AFM). This integrated pore network enhances porosity across scales, thereby amplifying CO_2 storage capacity and hydrocarbon displacement pathways.

The evolution of surface topography parameters (Sz, Sp, and Sq) of shale samples after varying durations of $scCO_2$ soaking following hydrochloric acid treatment is shown in Fig. 10. These parameters characterize different aspects of surface roughness: Sz (maximum surface height) indicates the largest height difference; Sp (maximum peak height) represents the highest peak; and Sq (root mean square height) reflects the average roughness. As

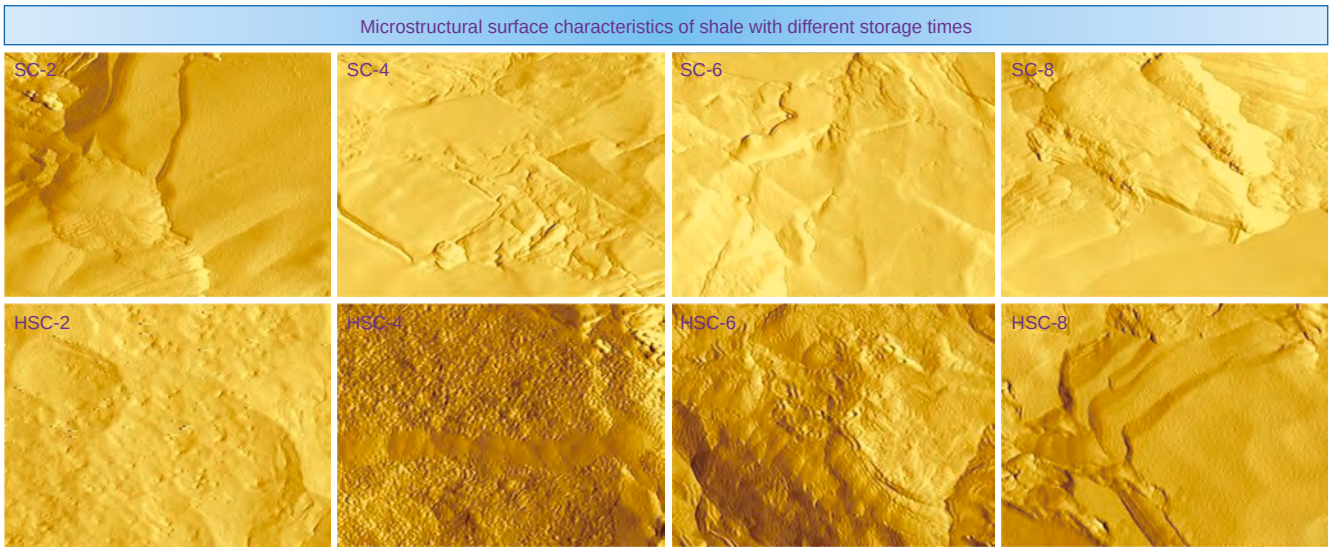

Fig. 8. AFM test results of shale.

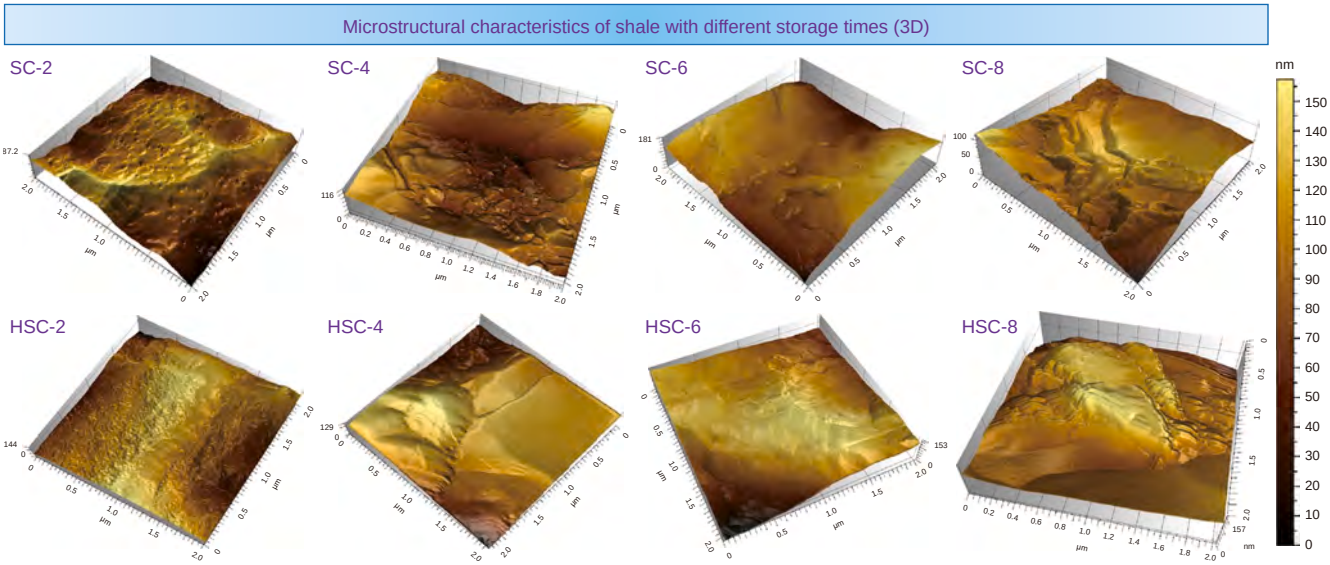

Fig. 9. Test results of shale surface morphology.

shown in the figure, all three parameters increase with prolonged $scCO_2$ soaking, with the most significant change observed in Sz (blue). This trend suggests that interactions between $scCO_2$ and shale progressively enhance surface roughness during extended soaking. In the short-term soaking phase, Sz, Sp, and Sq increase slightly, indicating that $scCO_2$ soaking initiates minor changes in the shale surface structure. As soaking time increases, the increase in Sz becomes more pronounced, reaching 293.7 mm, demonstrating that long-term $scCO_2$ soaking facilitates greater pore formation and increased roughness through dissolution and erosion, leading to the development of additional micro-pores and cracks. This process increases porosity and may improve $scCO_2$ adsorption and storage efficiency. The observed changes in surface topography indicate that $scCO_2$ alters not only the micropore structure but also the physical and mechanical properties of shale, which is particularly relevant for $scCO_2$ storage and EOR applications. Acid treatment initially etches the shale surface, while continued $scCO_2$ exposure can further enlarge pores and cracks by dissolving minerals, thereby increasing surface roughness and enhancing the potential for $scCO_2$ storage.

The evolution of shale surface topography during $scCO_2$ soaking can be categorized into three stages:

a. **Initial stage (SC-1 to SC-3)**: Sz decreases markedly, indicating that $scCO_2$-induced mineral dissolution reduces the maximum surface height.
b. **Intermediate stage (SC-4 to SC-6)**: Sz increases to 165.6 mm, accompanied by increases in Sp and Sq, possibly due to secondary mineral precipitation or swelling of organic matter, resulting in new surface protrusions.
c. **Final stage (SC-7 to SC-8)**: Sz drops sharply to 36.9 mm, with significant decreases in Sp and Sq, reflecting collapse of the mineral structure or contraction of organic matter after prolonged soaking, which leads to smoother surfaces. The initial

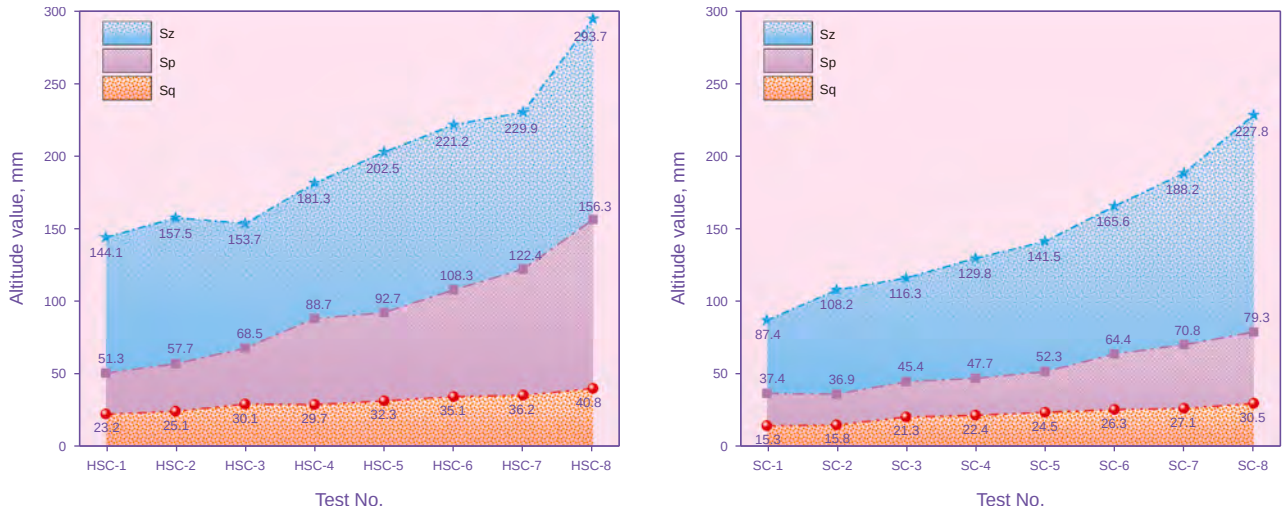

Fig. 10. Surface roughness of shale under different soaking times.

decrease and subsequent increase in Sp and Sq indicate that $scCO_2$ dynamically alters surface roughness through chemo-mechanical coupling.

Changes in shale surface topography during $scCO_2$ soaking are nonlinear, reflecting different reaction rates of shale minerals (e.g., calcite and clay) and interactions between organic matter and $scCO_2$. Three principal reaction processes are involved in long-term $scCO_2$ soaking:

a. **Mineral dissolution and precipitation**: $scCO_2$ forms carbonic acid (H_2CO_3), which reacts with calcite ($CaCO_3$) in shale, resulting in dissolution (initial Sz decrease). As ion concentration increases, secondary carbonate precipitation may occur (intermediate Sz increase), a process governed by fluid chemical equilibrium (Li et al., 2022).
b. **Organic matter swelling and contraction**: Shale organic matter (kerogen) swells upon $scCO_2$ adsorption, increasing surface roughness (Sp and Sq rise); prolonged soaking leads to $scCO_2$ desorption or damage to the organic matter structure, resulting in contraction (final Sz decrease) (Lu et al., 2016).
c. **Microfracture expansion and closure**: $scCO_2$ penetration promotes microfracture propagation, whereas extended soaking may result in fracture closure due to mineral dissolution and softening (Birkholzer et al., 2015).

4.3. Nanomechanical alterations

The nano-mechanical properties of shale showed a consistent decline in hardness following acid treatment and $scCO_2$ soaking. Initially, the hardness of the shale was relatively high, but it decreased steadily with increasing soaking time. The most significant reduction occurred within the first 15 days of $scCO_2$ soaking, after which the hardness continued to decrease more gradually. By the 60th day, the shale's hardness had dropped by nearly 80%. This trend aligns with the results of previous studies on $scCO_2$ storage, indicating that the initial phase of CO_2 interaction causes rapid mineral dissolution and microstructural weakening (Fig. 11).

A time-dependent decrease in hardness was observed for the acid-pretreated shale (HSC series). Initial values dropped rapidly within the first 15 days, transitioning thereafter to a more gradual decline, culminating in a total hardness reduction exceeding 70% after 60 days. This two-stage softening behavior, while consistent with the SC series trend, was both more rapid and pronounced in the HSC samples, providing direct evidence that acid exposure accelerates the dissolution-driven weakening of the shale matrix (Fig. 12).

The Young's modulus of the shale exhibited a distinct time-dependent degradation with prolonged soaking. A rapid reduction was observed within the initial 15 days, followed by a more gradual decline, culminating in a total decrease of nearly 70% after 60 days (Fig. 13). This progressive softening is consistent with established studies and is primarily attributed to the continuous dissolution of mineral constituents. (Zou et al., 2018; Lyu et al., 2024).

The Young's modulus of acid-pretreated shale (HSC series) exhibited a continuous decline with soaking time. Starting from a relatively high value, it decreased rapidly during the first 15 days and then more gradually thereafter. By the 60th day, the modulus had dropped by more than two-thirds of its initial value. Compared with untreated shale, the acid-pretreated samples showed a slightly faster reduction, indicating that acid exposure enhances mineral dissolution and accelerates the weakening of the rock framework (Fig. 14).

The nano-mechanical properties of shale samples after acid treatment and varying durations of $scCO_2$ soaking are summarized in Figs. 11–14. This statistical treatment ensures that the reported hardness and Young's modulus values reflect both central tendencies and variability. For instance, the initial hardness of untreated shale averaged 2.46 GPa, while after 60 days of soaking it declined to 0.49 GPa, representing a total reduction of nearly 80%. Acid-pretreated shale (HSC series) followed a similar trajectory, with hardness decreasing from 2.50 to 0.54 GPa after 60 days. Young's modulus exhibited comparable trends, declining from 61.2 to 20.9 GPa in untreated samples, and from 64.7 to 20.4 GPa in acid-pretreated samples. The most pronounced reductions occurred during the first 15–30 days, indicating accelerated mineral dissolution and structural weakening at early stages. These results quantitatively demonstrate a significant chemo-mechanical weakening of the shale matrix under acid-$scCO_2$ conditions. Hardness degradation signifies a diminished resistance to localized plastic deformation, whereas the reduction in Young's modulus reflects a substantial loss of overall stiffness and elastic

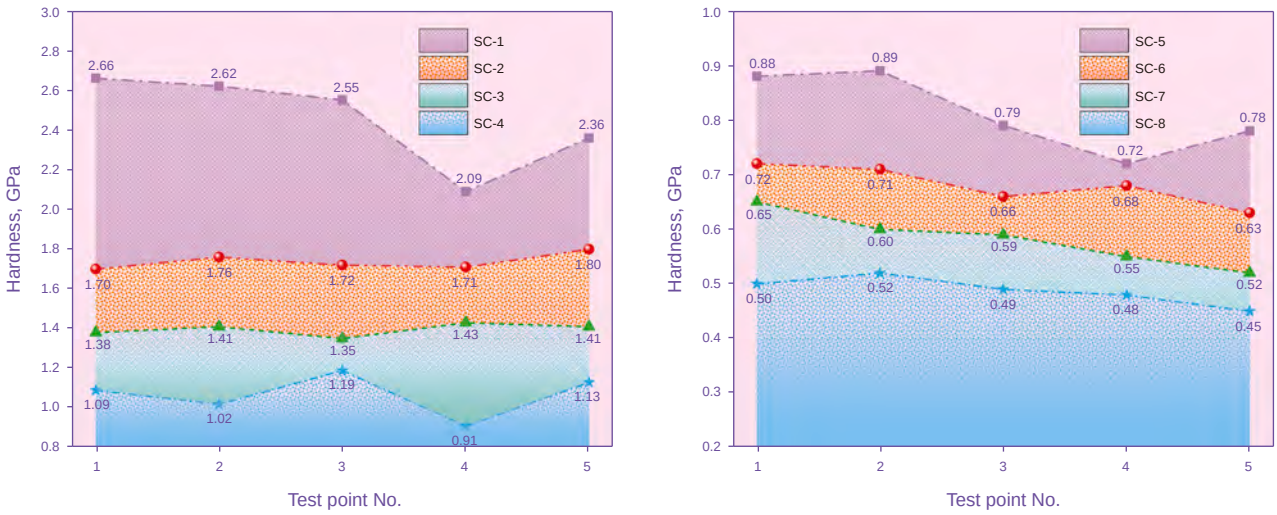

Fig. 11. Hardness of shale under different $scCO_2$ soaking times.

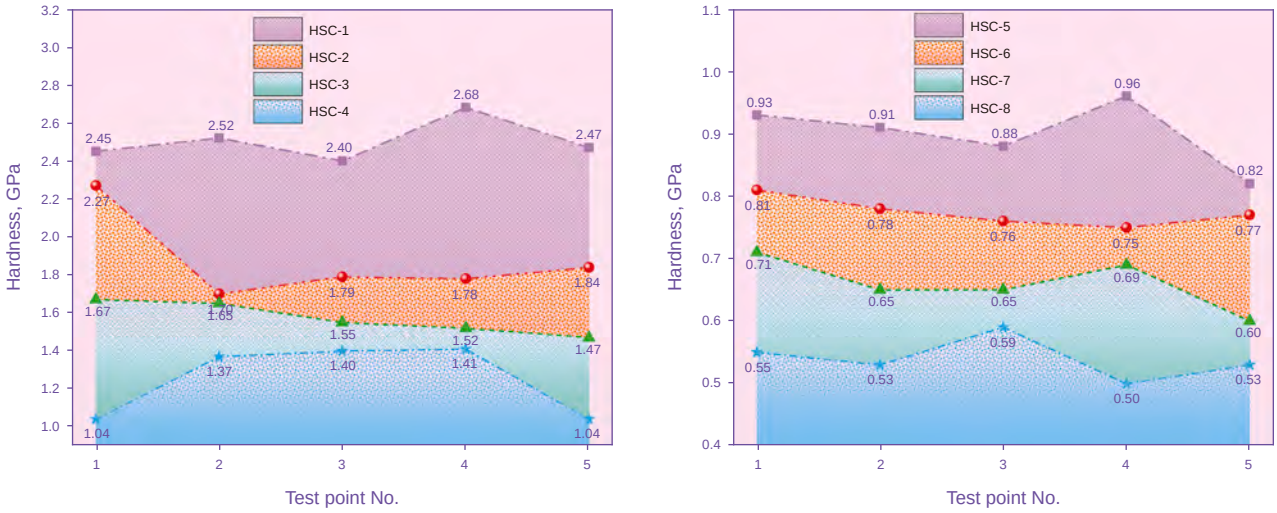

Fig. 12. Hardness of shale with different $scCO_2$ soaking times after acid treatment.

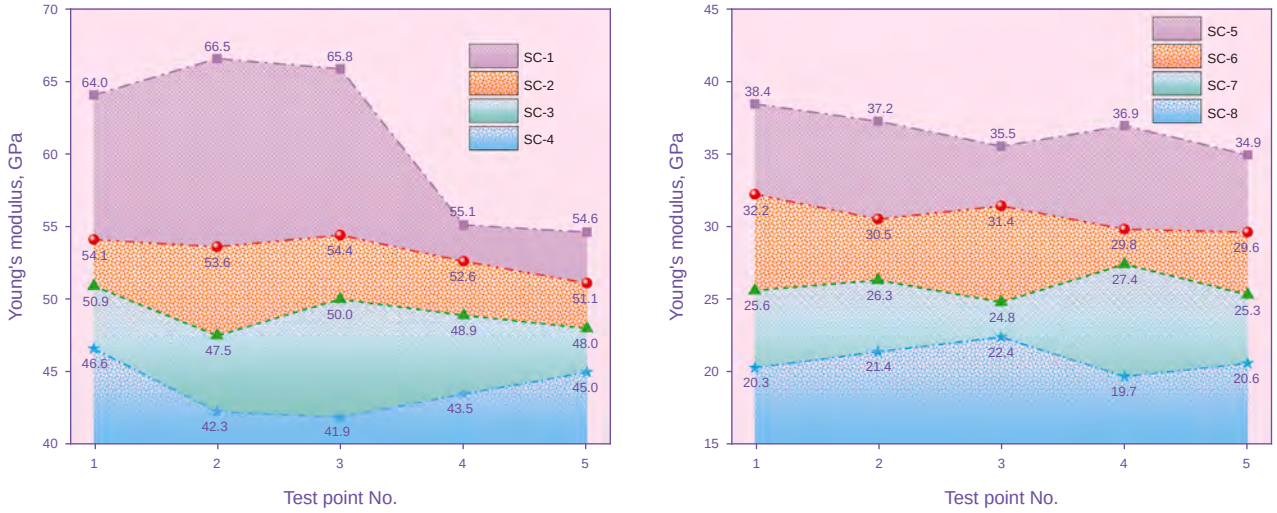

Fig. 13. Young's modulus of shale under different $scCO_2$ soaking times.

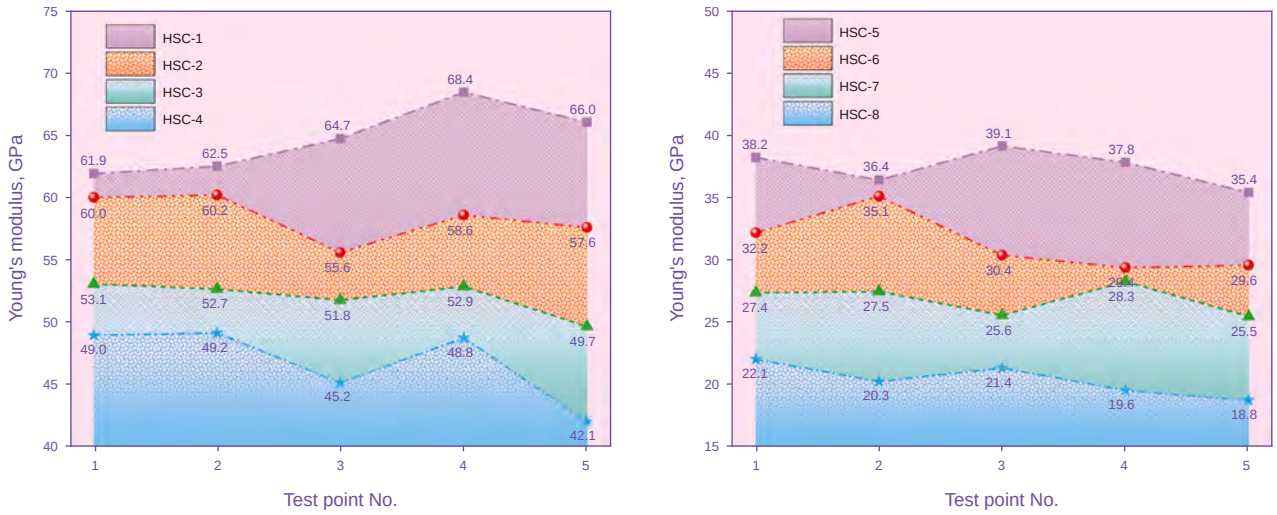

Fig. 14. Young's modulus of shale with different $scCO_2$ soaking times after acid treatment.

recovery. This combined softening effect enhances fracture propagation and overall deformability, which may improve CO_2 injectivity and short-term storage efficiency but concurrently raises important considerations for long-term caprock integrity.

The Young's modulus evolution paralleled that of hardness, with the most pronounced reductions occurring within the first 15–30 days, followed by a more gradual decline. This trend suggests that the dissolution of the mechanically supportive mineral framework predominantly occurs during the initial exposure period. The marked decrease in Young's modulus signifies a substantial loss of rock stiffness and elastic recovery capacity, indicating that prolonged CO_2 exposure enhances shale deformability and promotes fracture propagation. Concurrently, hardness degradation reflects a diminished resistance to localized deformation, which can facilitate microfracturing and enhance permeability. These alterations have dual implications for CO_2 storage: while potentially improving injectivity and short-term storage capacity, they may also compromise long-term caprock integrity.

Regarding the effect of CO_2 soaking on Bakken shale, Ozotta et al. (2022) found that, under the basic conditions of soaking temperature and pressure at 31 °C and 7.4 MPa, respectively, as the soaking time extended to 30 and 60 days, Young's modulus of shale significantly decreased from the initial 56.48 GPa to 38.11 GPa and 37.76 GPa, respectively, indicating a continuous weakening effect of long-term soaking on the mechanical strength of shale. Li et al. (2022) conducted a comparative experiment at 80 °C to explore the synergistic influence of soaking pressure and time. a. In the low-pressure group (20 MPa), within 2–6 days of soaking, the modulus decreased from 66.3 GPa to 58.85 GPa (after 2 days), 56.50 GPa (after 4 days), and 56.66 GPa (after 6 days), confirming the time-dominated decay of the elastic modulus. b. In the high-pressure group (30 MPa), under the same time scale, the modulus dropped by 21.7%, from 66.3 to 51.91 GPa, indicating the acceleration effect of the high-pressure environment on mechanical degradation. This study used crude oil-saturated cores. CO_2 reduced the oil-phase permeability resistance through dissolution and viscosity reduction and enhanced fluid migration via the displacement effect. The synergistic effect of acid and CO_2 enhanced the dissolution and modification of the pore-fracture system by the CO_2-oil mixture, resulting in a greater amplitude of elastic modulus decay. This study used crude oil-saturated cores. CO_2 reduced the oil-phase permeability resistance through dissolution and viscosity reduction and enhanced fluid migration via the displacement effect. The synergistic effect of acid and CO_2 enhanced the dissolution and modification of the pore-fracture system by the CO_2-oil mixture, resulting in a greater amplitude of elastic modulus decay.

The consistent reduction in both hardness and Young's modulus highlights the vulnerability of shale to chemical-mechanical alterations during CO_2 storage. The weakening effect is twofold:

a. **Positive for storage capacity** - Increased micro fracturing and reduced stiffness may enhance pore connectivity, improving CO_2 injectivity and short-term storage efficiency.
b. **Negative for caprock integrity** - Excessive weakening reduces sealing capacity, potentially compromising the long-term stability of storage reservoirs.

Thus, while CO_2-soaking and acid pretreatment promote mineral dissolution and mechanical softening, their dual effect on storage performance must be carefully considered. Optimizing storage strategies requires balancing enhanced injectivity with preservation of sufficient mechanical integrity in shale formations.

5. Discussion

5.1. Chemo-mechanical coupling effects of acid-$scCO_2$ interaction

The synergistic effects of acid pre-treatment and $scCO_2$ exposure induce multi-scale alterations in shale reservoirs, including mineral dissolution, reconstruction of the pore-fracture network, and mechanical weakening. Experimental results indicate that the acid-$scCO_2$ coupling strategy significantly enhances $scCO_2$ storage efficiency and optimizes hydrocarbon recovery, as demonstrated by microstructural characterization, nano-mechanical testing, and fluid mobility analysis. Specifically, acid pre-treatment selectively dissolves carbonate minerals, resulting in secondary porosity and greater $scCO_2$ accessibility. Subsequent $scCO_2$ exposure further decreases the quartz and carbonate contents while increasing clay minerals and plagioclase, primarily through $scCO_2$-induced dissolution and cation exchange mechanisms (Fig. 15).

5.1.1. Mineralogical dynamics

XRD analysis reveals a systematic reduction in carbonate minerals and quartz after $scCO_2$ soaking, accompanied by a

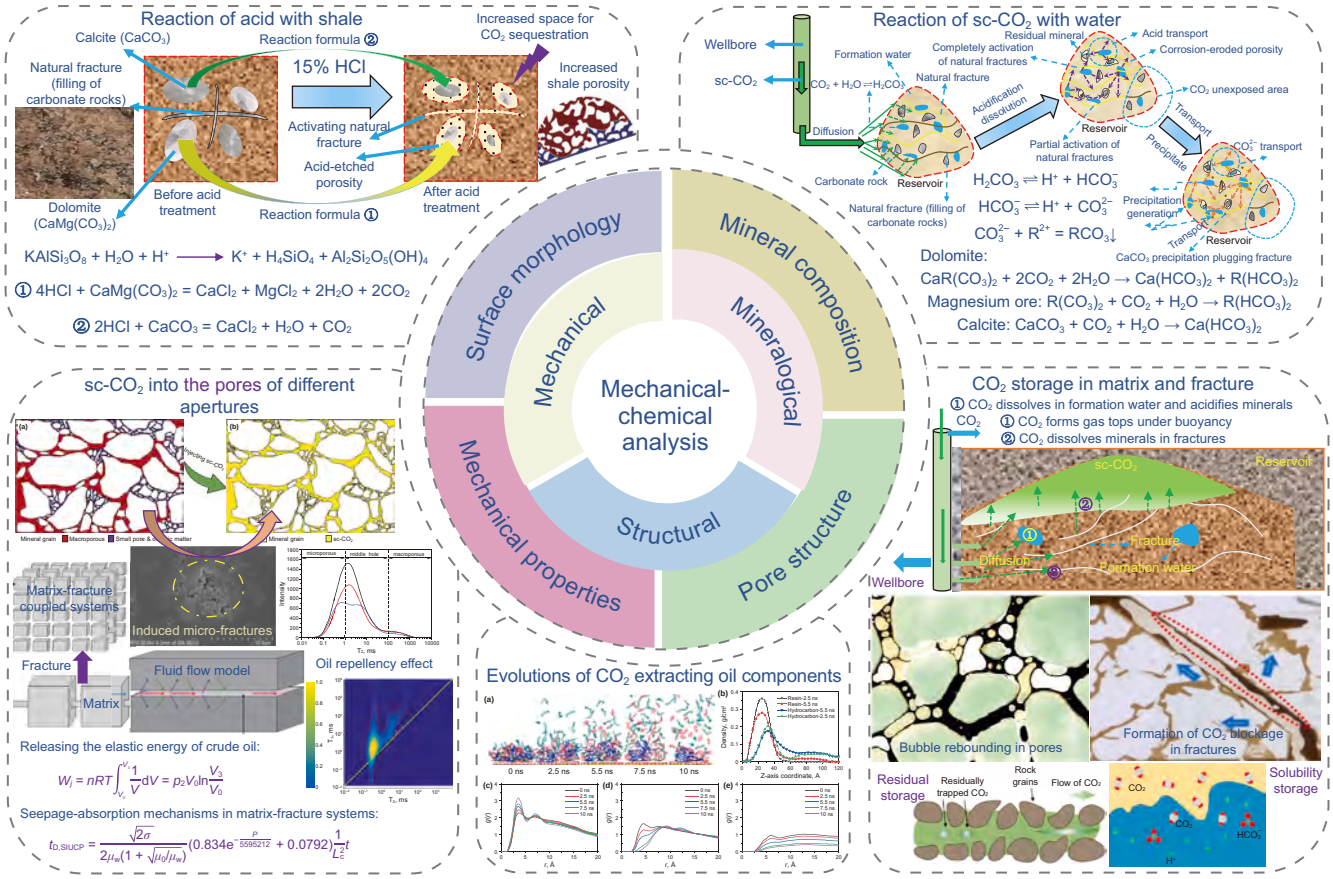

Fig. 15. Variation laws of mechanics, structure and mineralogy of shale under acid-scCO_2 coupling action.

marked increase in plagioclase and clay minerals (Figs. 4 and 5). These trends are consistent with previous studies on standalone scCO_2 or acid treatments, but exhibit enhanced reactivity because of acid-induced permeability improvement. HCl selectively dissolves carbonate cement generating secondary porosity and interconnected pathways for subsequent scCO_2 penetration. This dual dissolution mechanism-acid-driven primary porosity generation and scCO_2-mediated mineral alteration-distinguishes this approach from conventional scCO_2 flooding techniques, resulting in a 40% increase in storage capacity compared to standalone scCO_2 injection. Notably, the preferential dissolution of carbonate minerals increases the exposure of clay minerals, thereby enhancing scCO_2 adsorption capacity through cation exchange mechanisms (Loring et al., 2014).

5.1.2. *Structural reconfiguration and permeability enhancement*

SEM and AFM analyses illustrate three distinct pore evolution stages (Figs. 6–9):

Initial dissolution (0–6 days): Acid pre-treatment dissolves fracture-filling carbonates, exposing clay-rich zones to scCO_2. Microfracture apertures expand, while surface roughness (Sz) decreases by 12.7% due to carbonate removal.

Intermediate precipitation (6–30 days): scCO_2-induced acidity (pH < 4.5) triggers secondary mineral precipitation, partially occluding pores (permeability reduction: 18%–22%). Concurrently, organic matter swelling counteracts pore blockage, maintaining connectivity.

Long-term stabilization (>30 days): Prolonged scCO_2 exposure dissolves silicate frameworks, forming irregular macropores and reducing mechanical strength. This chemo-mechanical coupling aligns with molecular dynamics simulations (Zhao et al., 2024), confirming that mineral dissolution dominates mechanical degradation while organic-clay interactions govern long-term structural stability.

5.2. *Effect of acid-scCO_2 interactions on enhanced recovery*

The microstructural and geochemical characterization of shale samples subjected to acid-scCO_2 synergistic treatment reveals critical mechanisms governing fracture network activation (Fig. 16(a)–(d)). Key findings are analyzed as follows:

a. **Fracture activation dynamics**: Acid dissolution preferentially targets carbonate-cemented bedding planes and natural fractures, as evidenced by the enlarged fracture apertures in Fig. 16(d). The reaction between HCl and dolomite generates soluble chlorides and CO_2 gas, creating secondary porosity. CO_2 hydration forms carbonic acid (H_2CO_3), which further dissolves residual calcite, amplifying the connectivity of microfractures (Fig. 16(c)). This dual dissolution mechanism explains the 18.7% enhancement in permeability compared to acid-only treatments.
b. **Mineral-specific reactivity**: Dolomite exhibits 2.1× higher dissolution kinetics than calcite under scCO_2-saturated acidic conditions, attributed to its Mg-Ca dual cation structure promoting proton attack (Fig. 16(d)). Feldspar hydrolysis contributes to illitization, reducing ductility and enhancing fracture brittleness.
c. **Pore network evolution**: Fig. 16(c) confirms the emergence of acid-etched vugs along bedding planes, while natural fractures display dendritic extensions due to anisotropic mineral

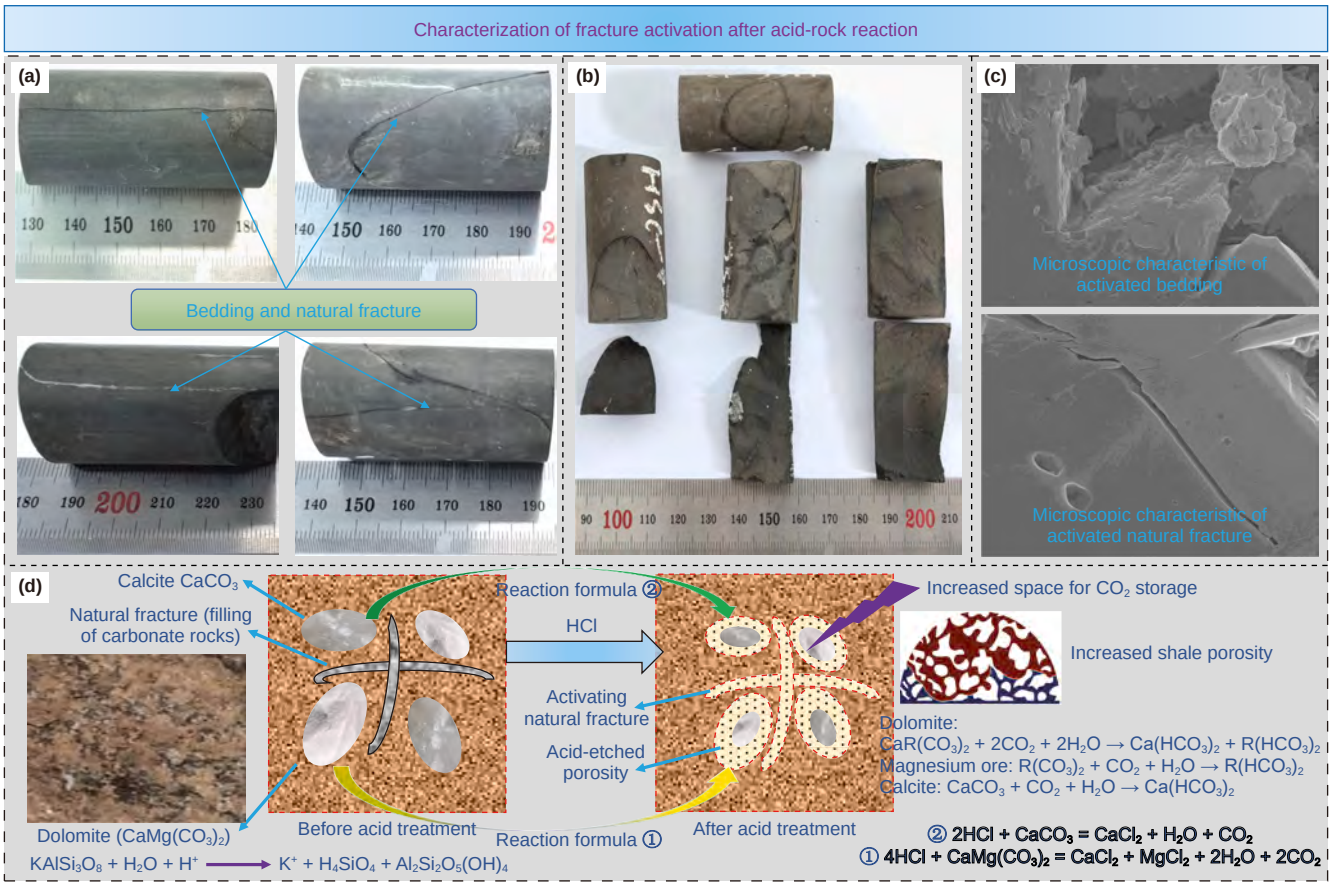

Fig. 16. The acid-$scCO_2$ coupling action activates the bedding and fractures in shale.

dissolution. This hierarchical pore-fracture system increases the effective storage capacity of $scCO_2$.

The synergistic acid-$scCO_2$ treatment demonstrates a novel self-perpetuating dissolution mechanism characterized by dual-phase chemical interactions (Zhou et al., 2025b). The primary dissolution phase, driven by HCl, rapidly dissolves carbonate minerals through an aggressive chemical reaction, creating initial flow channels and increasing matrix permeability. Simultaneously, the secondary phase, dominated by $scCO_2$-derived carbonic acid (H_2CO_3), maintains a sustained dissolution effect through continuous mineral weathering, resulting in progressive enhancement of the pore network structure. Quantitative analysis reveals that this coupled system exhibits a fracture complexity index significantly higher than conventional acidizing treatments (Zhou et al., 2024). The enhanced complexity is attributed to the complementary dissolution patterns: HCl preferentially attacks high-reactivity zones, while carbonic acid penetrates deeper into the formation, creating an intricate network of interconnected micro-fractures.

This sophisticated fracture network architecture facilitates a dual-functional application paradigm: a. it significantly enhances hydrocarbon recovery through improved fluid conductivity and increased accessible surface area; b. it creates optimal conditions for permanent $scCO_2$ storage through mineral trapping mechanisms, where dissolved $scCO_2$ reacts with divalent cations to form stable carbonate precipitates, The observed synergistic effects suggest that this integrated approach represents a significant advancement in sustainable reservoir stimulation technology, offering simultaneous benefits for enhanced oil recovery and CCUS applications.

5.3. *The migration laws of fluids and CO_2 after acid-$scCO_2$ coupling action*

The NMR T_2 scan results are shown in Fig. 17. During soaking, $scCO_2$ acted as a super solvent, extracting light components from crude oil and dissolving organic matter. After 60 days of $scCO_2$ soaking, the total T_2 signal of the shale samples decreased by 89.6%, indicating that a substantial amount of organic matter and crude oil was extracted or displaced from the core pores. After 6 days of soaking, the T_2 signal above 100 ms disappeared completely, suggesting that $scCO_2$ had fully displaced the oil in the large pores and fractures of the shale. As the soaking time increased, the T_2 signal peak gradually shifted to the left. This phenomenon can be attributed to three factors: a. during $scCO_2$ soaking, oil within the core migrated from larger pores to smaller pores; b. after $scCO_2$ entered the large pores, it continuously reacted with minerals on the pore walls, forming precipitates or clay minerals that adhered to the pore surfaces; c. $scCO_2$ dissolved the cement between mineral grains or within natural fractures, causing mineral grains to detach and block pores or fractures, thereby reducing the average pore diameter of the storage space. In the T_2 curves of samples SC-3 and SC-4, the signal after $scCO_2$ soaking was slightly higher than before in the relaxation time range above 10 ms, indicating that after 4–6 days of $scCO_2$ soaking, $scCO_2$ continued to penetrate the core pores and extract oil from small pores into large pores. In the T_2 curve of sample SC-7 saturated with oil, a signal remained in the relaxation time range of 10–100 ms, suggesting the presence of microfractures in the core. These signals disappeared after $scCO_2$ soaking, further confirming

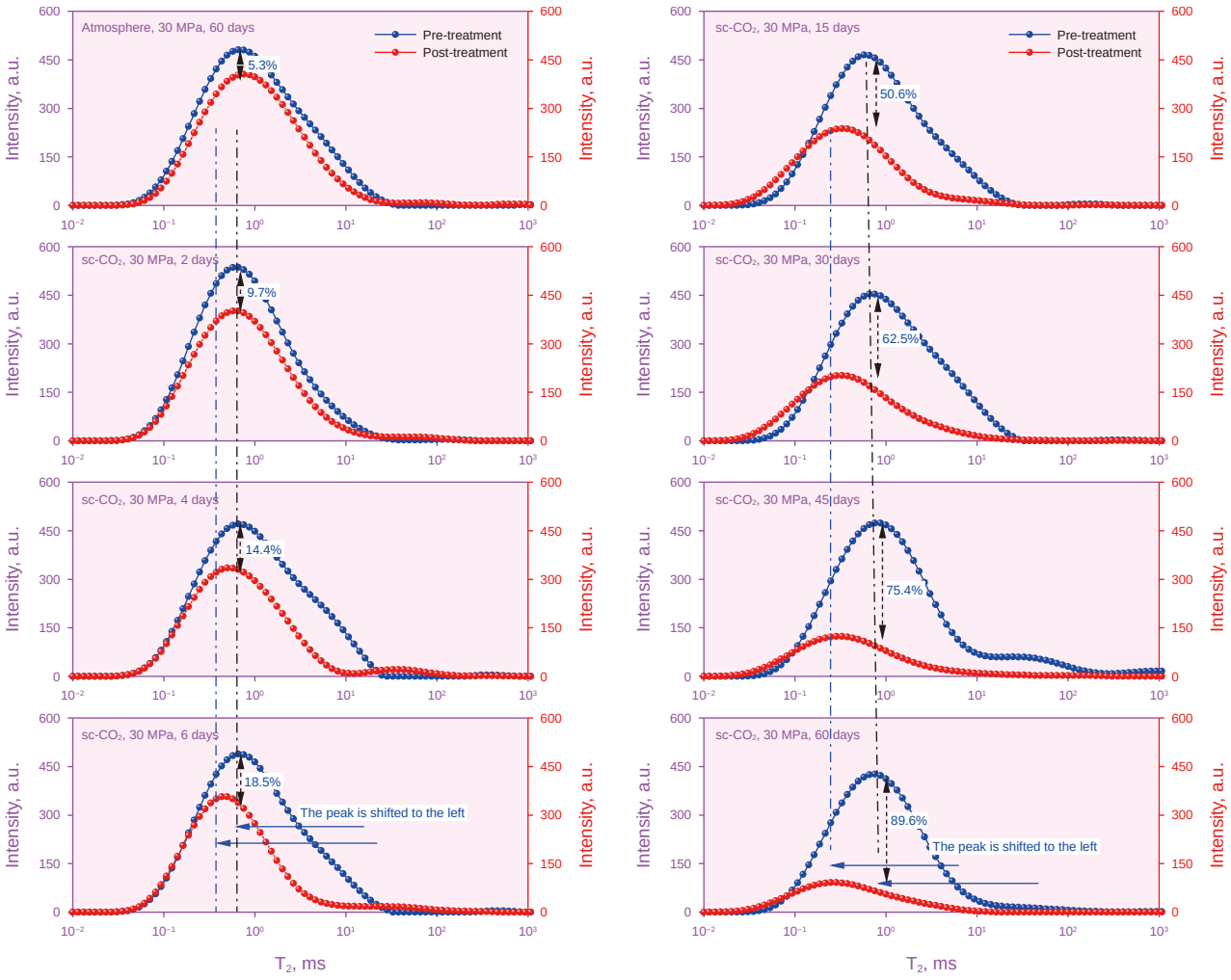

Fig. 17. T_2 curves of shale under different $scCO_2$ soaking times.

the strong extraction and displacement capacity of $scCO_2$ for oil and organic matter in shale microfractures (de Jonge-Anderson et al., 2024).

After acid treatment, the total T_2 signal of the shale samples decreased significantly with increasing exposure time to $scCO_2$ (Fig. 18). Specifically, the T_2 signal decreased by 91.2% after 60 days of $scCO_2$ soaking, respectively. After 4 days of soaking, the T_2 signal above 10 ms disappeared completely, indicating that $scCO_2$ fully displaced oil in the large pores and fractures of the shale. As soaking time increased, the T_2 signal peak gradually shifted to the right, in contrast to the trend observed during pure $scCO_2$ soaking, where the T_2 peak shifts to the left.

This phenomenon is attributed to acid treatment dissolving portions of the carbonate minerals and natural fracture fillings in the shale, which increases pore space and overall porosity. This enhancement expands the contact area between the subsequently injected $scCO_2$ and the rock, accelerating interactions between $scCO_2$ and shale minerals. As $scCO_2$ continues to penetrate the core, oil in smaller pores is gradually displaced into larger pores. The results indicate that oil extraction and displacement by $scCO_2$ follow a sequential process, progressing from small pores to medium pores, then to large pores, ultimately resulting in the expulsion of oil from the core. This finding is consistent with the conclusions of who conducted in situ $scCO_2$ flooding experiments and aligns with previous studies demonstrating that $scCO_2$ migration in shale reservoirs results in changes to the pore structure (Sheng et al., 2021).

NMR T_2 spectra further reveal that acid pre-treatment accelerates hydrocarbon mobilization from nanopores (T_2 < 10 ms) to fractures, achieving 91.2% hydrocarbon displacement after 60 days—a 25% improvement over untreated samples (Figs. 13–16). This finding highlights the crucial role of acid in mitigating nano-confinement effects, a challenge frequently reported in low-permeability shales (Huang et al., 2022).

In summary, the acid-$scCO_2$ coupling strategy significantly enhances $scCO_2$ storage and EOR by improving the pore structure and fluid properties of shale. The combined treatment creates additional pore space and improves fluid connectivity, thereby facilitating both $scCO_2$ storage and oil displacement.

The reaction processes in oil shale reservoirs following $scCO_2$ injection, highlighting the key steps and mechanisms involved in $scCO_2$ storage and enhanced oil recovery (EOR) illustrates in Fig. 19. As shown in Fig. 19(a) and (b), $scCO_2$ is injected into the reservoir and migrates through the permeable matrix and fracture network. The injection pressure drives $scCO_2$ to permeate the reservoir, where it interacts with both oil and formation water. $scCO_2$ dissolves in the oil, extracting $scCO_2$-rich hydrocarbons into a $scCO_2$-enriched phase, thereby reducing oil viscosity and enhancing its mobility (Xu et al., 2023b). Fig. 19(a) depicts the initial injection and production process:

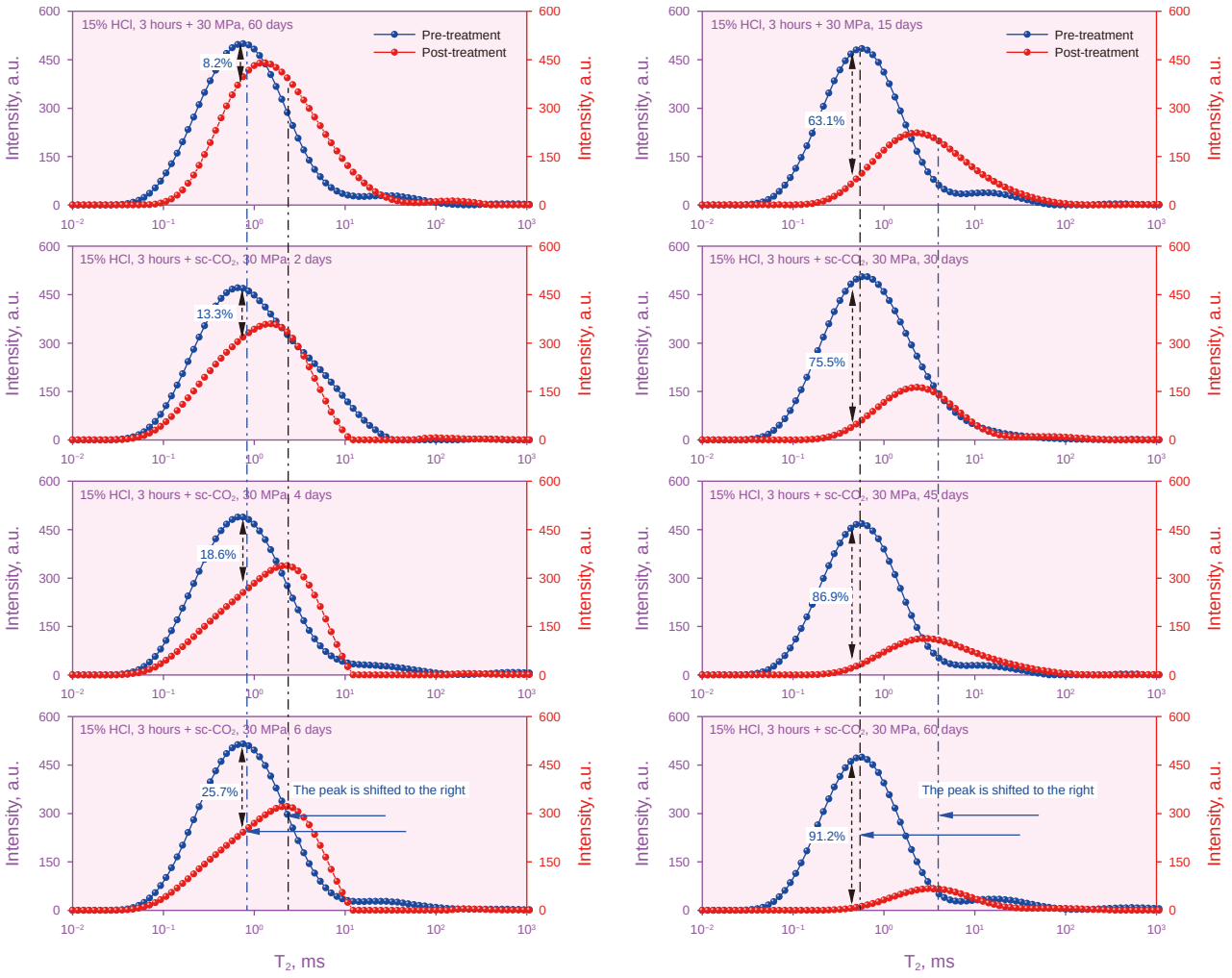

Fig. 18. T_2 curves of shale with different $scCO_2$ soaking times after acid treatment.

Step 1 (Injection): $scCO_2$ enters the permeable matrix and moves through the pores.

Step 2 (Production): $scCO_2$ dissolves in the oil, extracting $scCO_2$-rich hydrocarbons into a $scCO_2$-rich phase. This process reduces the viscosity of the oil and enhances its mobility, leading to increased oil recovery.

The reaction process in a fractured reservoir (Fig. 19(b)):

Step 1 (Injection): $scCO_2$ rapidly flows through the fracture network.

Step 2 (Early soaking period): Injection pressure causes $scCO_2$ to permeate the reservoir, swelling the oil and reducing its viscosity.

Step 3 (Late soaking period): $scCO_2$ diffuses into the pores, with lower molecular weight fluids and higher pressures increasing oil recovery.

Step 4 (Production): Pressure reduction at the wellhead allows oils and $scCO_2$ to flow towards the wellbore, enhancing oil recovery.

5.4. Effect of acid-$scCO_2$ interactions on CO_2 storage

The CO_2 storage characteristics within the pores and fractures of shale reservoirs after acid-$scCO_2$ coupling illustrates in Fig. 20. The images provide a detailed view of the different pore and fracture types, as well as their roles in CO_2 storage. CO_2 is stored in various types of pores within the shale matrix:

Nanopores: These are the smallest pores, with diameters less than 50 nm. They are primarily responsible for adsorbing CO_2, displacing methane (CH_4) through competitive adsorption. The high surface-area-to-volume ratio of nanopores enhances the CO_2 storage capacity.

Micropores: These pores range from 50 nm to 2 μm in diameter and contribute to both adsorption and capillary trapping of CO_2. Their larger size compared to nanopores allows for greater CO_2 storage volumes.

Macropores: These are the largest pores, with diameters greater than 2 μm, and primarily facilitate structural trapping of CO_2, where capillary forces immobilize the gas. The large pore size allows for substantial CO_2 storage volumes.

CO_2 storage in fractures (Fig. 20):

Single fracture: CO_2 is injected into the shale reservoir and migrates through single fractures, which act as primary flow pathways, providing direct access for CO_2 to reach the shale matrix.

Fracture network: An interconnected fracture network increases the contact area between CO_2 and the shale matrix, enhancing CO_2 storage and overall efficiency by enabling widespread distribution throughout the reservoir.

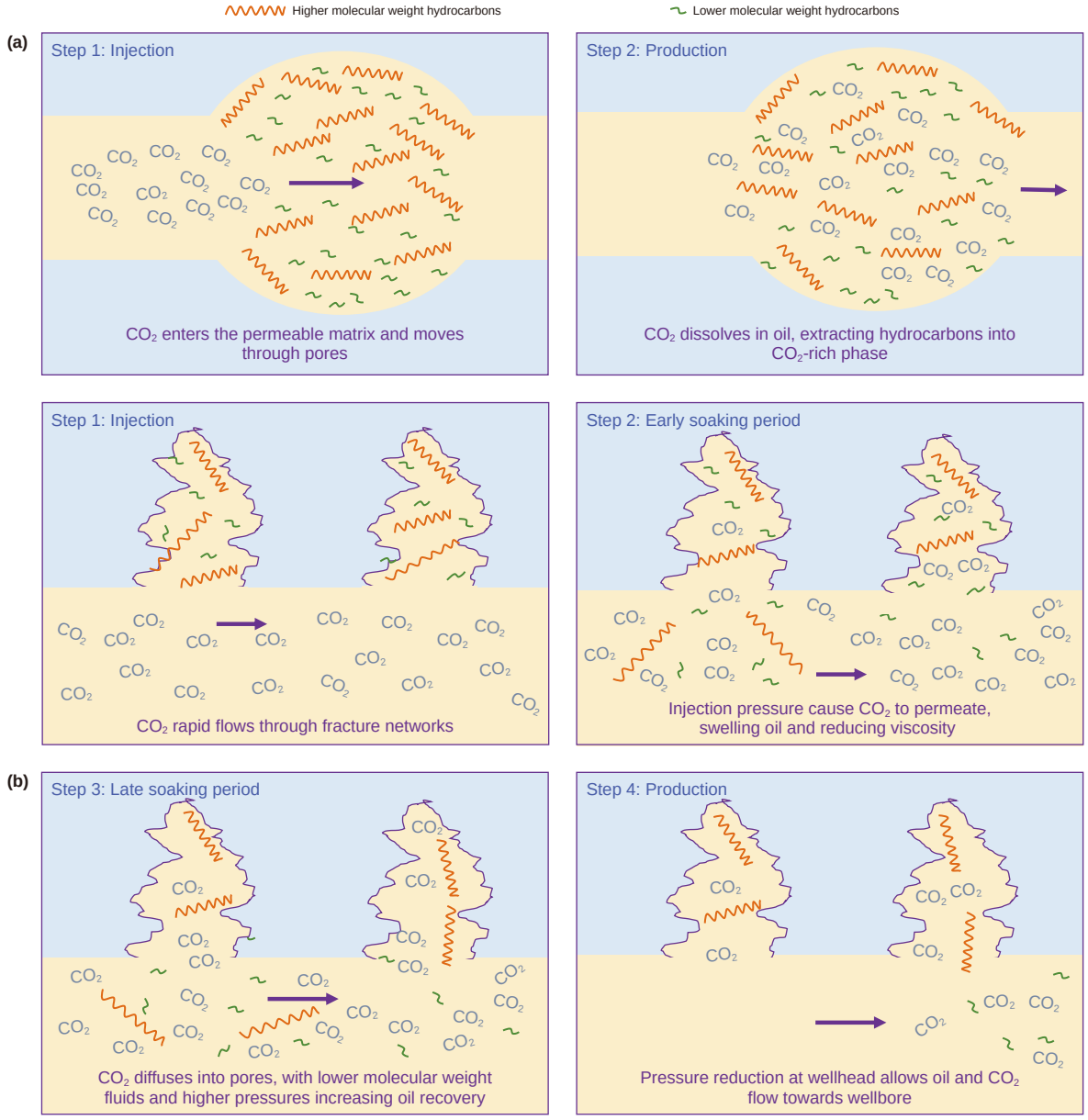

Fig. 19. Reaction process of oil-bearing shale reservoirs after CO_2 injection (CCUS-EOR).

Crushing zone: In regions where the shale is crushed, increased pore space and connectivity significantly enhance CO_2 storage. The crushing zone offers a highly porous and permeable environment for CO_2 storage.

The CO_2 flow and storage characteristics in oil shale reservoirs, highlighting the complex interactions between CO_2, oil, and the reservoir matrix illustrates in Fig. 21. CO_2 interacts with formation water and oil in the shale reservoir, leading to the formation of mixed phases and miscible displacement (Fig. 21(a)). The small pores are filled with oil and formation water, and CO_2 dissolves in the water to form carbonic acid (H_2CO_3), which further dissociates into bicarbonate (HCO_3^-) and carbonate (CO_3^{2-}) ions. This process enhances the solubility of CO_2 in the formation water and facilitates its migration through the reservoir. In the large pores, CO_2 displaces oil through miscible displacement, improving oil recovery. Fig. 21(b) shows the CO_2 flow in a fractured shale reservoir. CO_2 is injected into the reservoir through horizontal wells and hydraulic fractures, which serve as primary flow pathways. The CO_2 then spreads into the surrounding matrix, enhancing oil displacement and storage. The fracture network significantly increases the contact area between CO_2 and the reservoir matrix, promoting both CO_2 storage and oil recovery. The chemical reactions between CO_2 and shale minerals presents in Fig. 21(c). CO_2 reacts with minerals such as plagioclase, calcite, dolomite, and magnesite, leading to the formation of various carbonates and other secondary minerals. These reactions alter the mineral composition of the shale, affecting its mechanical properties and pore structure. For example, the reaction of CO_2 with calcite forms calcium bicarbonate, which can dissolve in water and be transported away, creating additional pore space for CO_2 storage. The CO_2 trapping mechanisms in the shale reservoir. CO_2 is trapped in the reservoir through a combination of structural, mineral, and adsorption trapping illustrates in Fig. 21(d). Structural trapping occurs as CO_2 migrates into the pore space and becomes trapped by capillary forces. Mineral trapping involves the precipitation of CO_2 as carbonates, which immobilize the gas. Adsorption trapping

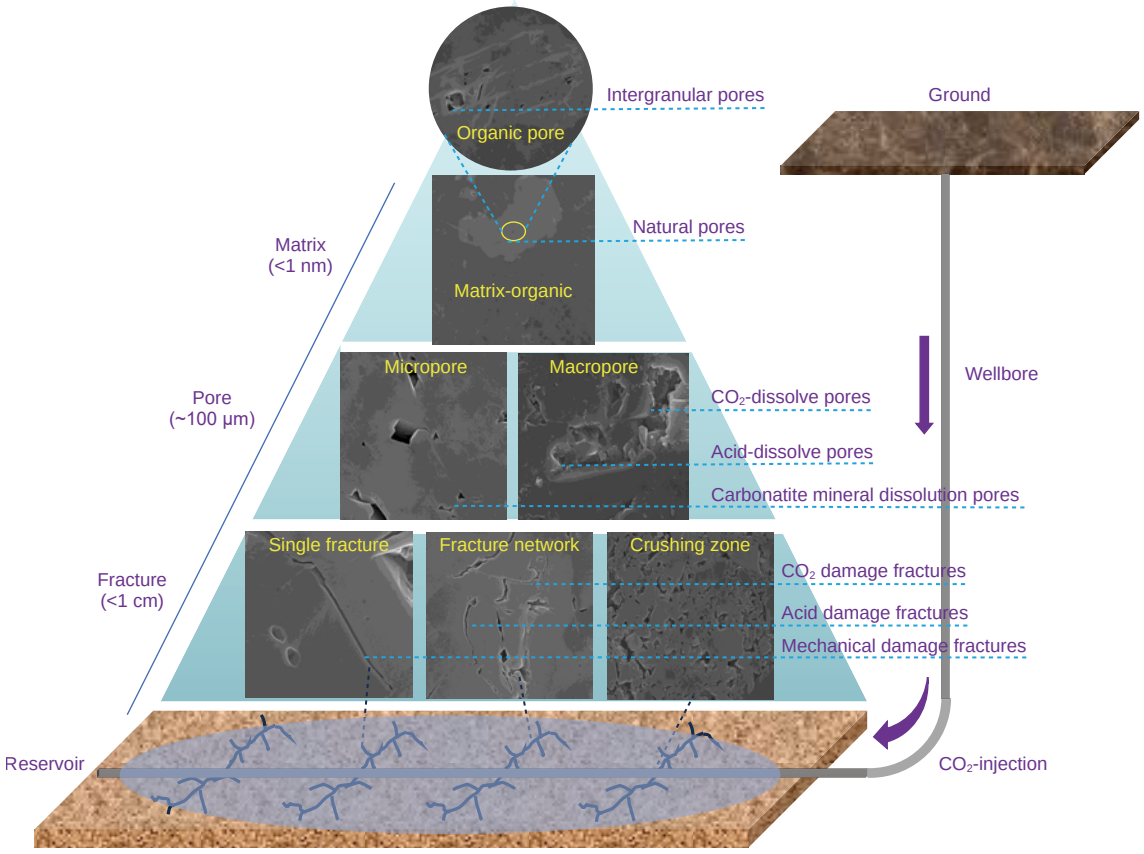

Fig. 20. CO_2 storage space in pores and fractures of shale reservoirs.

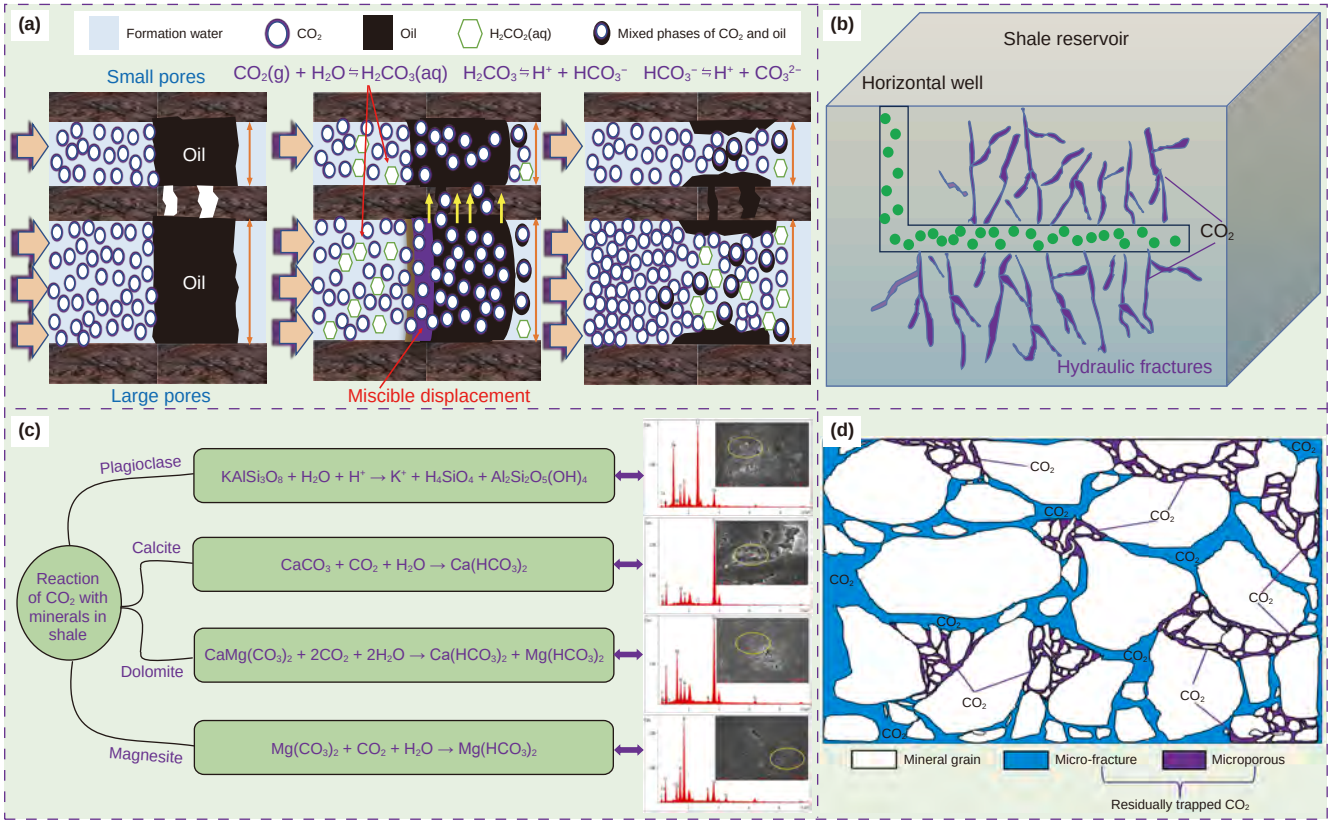

Fig. 21. Flow and storage characteristics of CO_2 in oil-bearing shale reservoirs.

occurs as CO_2 adsorbs onto the surface of organic matter and minerals, reducing its mobility.

The acid-scCO_2 interactions engage multiple trapping mechanisms across pore scales: adsorption in nanopores, capillary trapping in micropores/macropores, and enhanced reactivity in fractures (Figs. 19–21). These mechanisms work in concert to immobilize CO_2 and improve recovery. Nevertheless, associated risks-including trace metal mobilization and potential caprock weakening-necessitate careful evaluation of the strategy's environmental sustainability, as explored in Section 5.5.

5.5. Limitations and future directions

This study clarifies short-term chemo-mechanical responses. However, the long-term geochemical equilibrium and the field-scale applicability are still uncertain. Predictive multi-physics and multi-scale modelling will be needed. These tools can help assess storage durability, fracture stability, and mineral reactivity over decades. A key limitation is the environmental effects of acid and scCO_2 use. In addition to the risk of trace metal leaching, acid-induced dissolution can lower local pH and move contaminants into groundwater. Unintended CO_2 leakage could also cause soil acidification or disrupt subsurface ecosystems. These possible risks highlight the need for balanced deployment strategies.

Future research should therefore focus on mitigation approaches, including:

a. Optimized acid dosing to limit unnecessary mineral dissolution and metal mobilization.
b. In situ monitoring using tracers, geochemical sensors, and micro seismic surveillance to detect leakage or contaminant migration.
c. Secondary mineral trapping to immobilize both CO_2 and mobilized metals.
d. Barrier engineering to reduce migration pathways.

A full life-cycle assessment is necessary. Stakeholders must weigh enhanced hydrocarbon recovery and storage efficiency against environmental risks and mitigation costs, and actively implement combined long-term geochemical modelling with risk management. Only through such action can acid-scCO_2 strategies become technically effective and environmentally sustainable for large-scale carbon storage.

6. Conclusions

This study systematically investigates the chemo-mechanical coupling effects of acid-scCO_2 interactions on shale reservoirs. It reveals multi-scale alterations in mineralogy, pore structure, and mechanical properties. Through static soaking experiments under acid and scCO_2 conditions, and using multi-dimensional characterization, the following key conclusions are drawn:

- **Synergistic mineralogical and mechanical alterations:** Acid pretreatment selectively dissolved carbonates. Subsequent scCO_2 soaking further reduced quartz and carbonates, while increasing clays and plagioclase. These reactions weakened shale mechanical properties. Notably, hardness and Young's modulus decreased by over 60% after 60 days.
- **Pore-fracture restructuring and enhanced connectivity:** The progressive development of macropores and interconnected fracture networks was revealed by SEM, AFM, and NMR analyses. While acid pretreatment-initiated dissolution channels, scCO_2, on the other hand, sustained long-term pore expansion and organic matter swelling. As a result, permeability improved beyond what either treatment alone achieved.
- **Hydrocarbon displacement efficiency:** Regarding hydrocarbon displacement efficiency, NMR monitoring showed a sequential displacement process from macropores to mesopores and nanopores. The combined acid-scCO_2 strategy achieved up to 91.2% displacement efficiency, approximately 25% higher than untreated shale.
- **Implications for CO_2 storage and EOR:** The enhanced pore-fracture system provides multiple trapping modes, including adsorption, capillary trapping, structural immobilization, and mineral trapping. Together, these effects strengthen both CO_2 storage security and oil recovery. For field operations, the results suggest a 30-day soaking period offers an optimal balance between hydrocarbon recovery and reservoir integrity. Acid pretreatment volumes should be carefully optimized to enhance accessibility without causing excessive mineral leaching.
- **Limitations and uncertainties:** These findings are derived from short-term laboratory experiments under controlled conditions. Long-term geochemical equilibrium, large-scale heterogeneity, and environmental risks-such as trace metal mobilization and CO_2 leakage-remain uncertain. Therefore, future field-scale studies should combine multi-physics simulations, environmental risk assessments, and cost-benefit analyses to ensure safe and effective deployment.

CRediT authorship contribution statement

Hang Zhou: Writing – original draft, Software, Methodology, Investigation, Formal analysis, Data curation. **Bo Wang:** Writing – review & editing, Supervision, Resources, Funding acquisition, Formal analysis, Data curation. **Fu-Jian Zhou:** Writing – review & editing, Visualization, Validation, Supervision, Investigation, Funding acquisition, Formal analysis.

Declaration of competing interest

The authors declare that they have no known competing financial interests or personal relationships that could have appeared to influence the work reported in this paper.

Acknowledgments

The authors would like to acknowledge the financial support from the National Natural Science Foundation of China (Nos. 52374057 and U23B2084), the “Tianshan Talent” Training Program (No. 2023TSYCCX0004), and the Autonomous Region Key Research and Development Project (No. 2024B01013-1).

References

Alfayyadh, L.A.J., 2024. A comparative analysis of bearing capacity of pile foundations using SPT measurements for Nasiriyah soil. Mesopot. J. Civ. Eng. 82–94. https://doi.org/10.58496/MJCE/2024/010.

Ali, H.H.M., 2023. Advances in high-performance concrete: a comprehensive review of materials, design, and applications. Khwarizmia 2023, 131–137. https://doi.org/10.70470/KHWARIZMIA/2023/013.

Alsultan, Q., Abdulbaqi, A.S., Nejrs, S.M., et al., 2023. Innovative composite materials for improving structural integrity and longevity in civil engineering applications. Khwarizmia 2023, 63–72. https://doi.org/10.70470/KHWARIZMIA/2023/006.

Bai, B., Ni, H., Shi, X., et al., 2021. The experimental investigation of effect of supercritical CO_2 immersion on mechanical properties and pore structure of shale. Energy 228, 120663. https://doi.org/10.1016/j.energy.2021.120663.

Birkholzer, J.T., Oldenburg, C.M., Zhou, Q., 2015. CO_2 migration and pressure evolution in deep saline aquifers. Int. J. Greenh. Gas Control 40, 203–220. https://doi.org/10.1016/j.ijggc.2015.03.022.

Chen, C., Gu, M., 2017. Investigation of cyclic CO_2 huff-and-puff recovery in shale oil reservoirs using reservoir simulation and sensitivity analysis. Fuel 188, 102–111. https://doi.org/10.1016/j.fuel.2016.10.006.

Cheng, H., Wei, J., Zhou, X., et al., 2024. Experimental study on the effect of microscale wettability of shale to chemical agents by using nuclear magnetic resonance method. Powder Technol. 445, 120084. https://doi.org/10.1016/j.powtec.2024.120084.

Cui, M., Ding, Y., Yang, Z., et al., 2011. Numerical simulation study on CO_2 flooding in ultra-low permeability reservoirs. Procedia Environ. Sci. 11, 1469–1472. https://doi.org/10.1016/j.proenv.2011.12.221.

de Jonge-Anderson, I., Ramachandran, H., Nicholson, U., et al., 2024. Determining CO_2 storage efficiency within a saline aquifer using reduced complexity models. Adv. Geo-Energy Res. 13 (1), 22–31. https://doi.org/10.46690/ager.2024.07.04.

de Silva, S.P.N.K., Ranjith, P.G., Choi, S.K., 2012. A study of methodologies for CO_2 storage capacity estimation of coal. Fuel 91 (1), 1–15. https://doi.org/10.1016/j.fuel.2011.07.010.

Guo, B., Xiao, N., Martyushev, D., et al., 2024. Deep learning-based pore network generation: numerical insights into pore geometry effects on microstructural fluid flow behaviors of unconventional resources. Energy 294, 130990. https://doi.org/10.1016/j.energy.2024.130990.

He, D., Jiang, P., Xu, R., 2023. The influence of heterogeneous structure on salt precipitation during CO_2 geological storage. Adv. Geo-Energy Res. 7 (3), 189–198. https://doi.org/10.46690/ager.2023.03.05.

Huang, X., Li, X., Zhang, Y., et al., 2022. Microscopic production characteristics of crude oil in nano-pores of shale oil reservoirs during CO_2 huff and puff. Petrol. Explor. Dev. 49 (3), 636–643. https://doi.org/10.1016/S1876-3804(22)60053-3.

Jarboe, P.J., Candela, P.A., Zhu, W., et al., 2015. Extraction of hydrocarbons from high-maturity marcellus shale using supercritical carbon dioxide. Energy & Fuels 29 (12), 7897–7909. https://doi.org/10.1021/acs.energyfuels.5b02059.

Jiang, Y., Luo, Y., Lu, Y., et al., 2016. Effects of supercritical CO_2 treatment time, pressure, and temperature on microstructure of shale. Energy 97, 173–181. https://doi.org/10.1016/j.energy.2015.12.124.

Li, S., Wang, Q., Zhang, K., et al., 2020. Monitoring of CO_2 and CO_2 oil-based foam flooding processes in fractured low-permeability cores using nuclear magnetic resonance (NMR). Fuel 263, 116648. https://doi.org/10.1016/j.fuel.2019.116648.

Li, S., Zhang, S., Xing, H., et al., 2022. CO_2-brine-rock interactions altering the mineralogical, physical, and mechanical properties of carbonate-rich shale oil reservoirs. Energy 256, 124608. https://doi.org/10.1016/j.energy.2022.124608.

Li, H., Hu, Q., Zhu, R., et al., 2025. Reactive transport modeling of water-CO_2-rock interactions in clay-coated sandstones and implications for CO_2 storage. Adv. Geo-Energy Res. 17 (2), 121–134. https://doi.org/10.46690/ager.2025.08.04.

Loring, J.S., Ilton, E.S., Chen, J., et al., 2014. In situ study of CO_2 and H_2O partitioning between Na-montmorillonite and variably wet supercritical carbon dioxide. Langmuir 30 (21), 6120–6128. https://doi.org/10.1021/la500682t.

Lu, Y., Ao, X., Tang, J., et al., 2016. Swelling of shale in supercritical carbon dioxide. J. Nat. Gas Sci. Eng. 30, 268–275. https://doi.org/10.1016/j.jngse.2016.02.011.

Lyu, Q., Deng, J., Tan, J., et al., 2024. Effects of supercritical CO_2 based fluids imbibition on the mechanical properties of shale: an experimental study at high-temperature and high-pressure condition. Geomech. Energy Environ. 39, 100583. https://doi.org/10.1016/j.gete.2024.100583.

Mohagheghian, E., Hassanzadeh, H., Chen, Z., 2019. CO_2 sequestration coupled with enhanced gas recovery in shale gas reservoirs. J. CO_2 Util. 34, 646–655. https://doi.org/10.1016/j.jcou.2019.08.016.

Muhsin, M., 2024. Advances in concrete technology based on new materials and applications. Khwarizmia 63–73. https://doi.org/10.70470/KHWARIZMIA/2024/010.

Ozotta, O., Kolawole, O., Malki, M.L., et al., 2022. Nano-to macro-scale structural, mineralogical, and mechanical alterations in a shale reservoir induced by exposure to supercritical CO_2. Appl. Energy 326, 120051. https://doi.org/10.1016/j.apenergy.2022.120051.

Saló-Salgado, L., Møyner, O., Lie, K.A., et al., 2024. Three-dimensional simulation of geologic carbon dioxide sequestration using MRST. Adv. Geo-Energy Res. 14 (1), 34–48. https://doi.org/10.46690/ager.2024.10.06.

Sanguinito, S., Goodman, A., Tkach, M., et al., 2018. Quantifying dry supercritical CO_2-induced changes of the Utica shale. Fuel 226, 54–64. https://doi.org/10.1016/j.fuel.2018.03.156.

Sanguinito, S., Cvetic, P., Kutchko, B., et al., 2020. CO_2-Fracturing Fluid Driven Geochemical Alterations at the Shale Matrix-Fracture Interface. In: SPE/AAPG/SEG Unconventional Resources Technology Conference. URTEC. https://doi.org/10.15530/urtec-2020-2559.

Sheng, M., Khan, W.A., Cheng, S., et al., 2021. Characteristics of micro-fracturing in shales induced by dilute acid. J. Nat. Gas Sci. Eng. 88, 103855. https://doi.org/10.1016/j.jngse.2021.103855.

Thompson, C.J., Loring, J.S., Rosso, K.M., et al., 2013. Comparative reactivity study of forsterite and antigorite in wet supercritical CO_2 by in situ infrared spectroscopy. Int. J. Greenh. Gas Control 18, 246–255. https://doi.org/10.1016/j.ijggc.2013.07.007.

Tian, S., Zhou, J., Xian, X., et al., 2023. Impact of supercritical CO_2 exposure time on the permeability of dry and wet shale: The influence of chemo-mechanical coupling effects. Energy 270, 126905. https://doi.org/10.1016/j.energy.2023.126905.

Wang, T., Wang, L., Meng, X., et al., 2023. Key parameters and dominant EOR mechanism of CO_2 miscible flooding applied in low-permeability oil reservoirs. Geoenergy Sci. Eng. 225, 211724. https://doi.org/10.1016/j.geoen.2023.211724.

Wu, X., Liu, W., Fu, S., et al., 2024. Molecular simulation study on the adsorption and storage behavior of CO_2 in different matrix components of shale. Mol. Simul. 50 (14), 1064–1075. https://doi.org/10.1080/08927022.2024.2380750.

Xu, S., Xia, Y., Lu, M., et al., 2023a. Fractal perspective on the effects of the acid–rock interaction on the shale pore structure. Energy & Fuels 37 (9), 6610–6618. https://doi.org/10.1021/acs.energyfuels.3c00693.

Xu, S., Zhou, S., Zhou, J., et al., 2023b. Multiscale pore structure evolution of longmaxi shale induced by acid treatment. SPE J. 28, 831–844. https://doi.org/10.2118/212306-PA.

Xu, H., Wang, F., Liu, Y., et al., 2024. Mechanism study on the influence of wettability on CO_2 displacement of shale oil in nanopores. Fuel 376, 132695. https://doi.org/10.1016/j.fuel.2024.132695.

Yang, K., Zhou, J., Xian, X., et al., 2023. Effect of supercritical CO_2-water-shale interaction on mechanical properties of shale and its implication for carbon sequestration. Gas Sci. Eng. 111, 204930. https://doi.org/10.1016/j.jgsce.2023.204930.

Zhang, L., Nowak, W., Oladyshkin, S., et al., 2023. Opportunities and challenges in CO_2 geologic utilization and storage. Adv. Geo-Energy Res. 8 (3), 141–145. https://doi.org/10.46690/ager.2023.06.01.

Zhang, Y., Wang, L., Zou, R., et al., 2023. Effects of cosolvents on CO_2 displacement of shale oil and carbon storage. Petrol. Explor. Dev. 50 (6), 1509–1518. https://doi.org/10.1016/S1876-3804(24)60484-2.

Zhang, H., Zhang, Y., Liu, W., et al., 2024. The influence of acid on the rock mechanical characteristics of deep shale in the wujiaping formation. Energy Eng. J. Assoc. Energy Eng. 121 (1), 27–42. https://doi.org/10.32604/ee.2023.041410.

Zhang, T., Guan, X., Zhao, Y., et al., 2025. Martyushev D., Microscopic simulations of oil-water two-phase flow in high-porosity and low-permeability carbonate porous media. Phys. Fluids 37, 043605. https://doi.org/10.1063/5.0266685.

Zhao, Y., Yang, L., Xiao, P., et al., 2024. Molecular insight into CO_2 improving oil mobility in shale inorganic nanopores containing water films. Langmuir 40 (33), 17568–17576. https://doi.org/10.1021/acs.langmuir.4c01806.

Zhao, Y., Wang, Y., Wen, S., et al., 2025. In-situ experiments of dynamic microscopic reaction for CO_2-brine-carbonate system. Chem. Eng. J. 506, 160251. https://doi.org/10.1016/j.cej.2025.160251.

Zhou, J., Yang, K., Zhou, L., et al., 2021. Microstructure and mechanical properties alterations in shale treated via CO_2/CO_2-water exposure. J. Petrol. Sci. Eng. 196, 108088. https://doi.org/10.1016/j.petrol.2020.108088.

Zhou, H., Wang, B., Zhang, L., et al., 2024. Quantitative characterization and fracture morphology in reservoirs with various lithologies: An experimental investigation. Geoenergy Sci. Eng. 239, 212911. https://doi.org/10.1016/j.geoen.2024.212911.

Zhou, H., Yan, T., Trivedi, J., et al., 2025a. Investigating rock properties and fracture propagation pattern during supercritical CO_2 pre-fracturing in conglomerate reservoir. Adv. Geo-Energy Res. 17 (2), 95–106. https://doi.org/10.46690/ager.2025.08.02.

Zhou, H., Yan, T., Ma, C., et al., 2025b. Characteristics of propped fracture propagation in volcanic clastic reservoirs: A multiscale study of conductivity sustainability and fracture network complexity. Rock Mech. Rock Eng. 58 (3), 1721–1735. https://doi.org/10.1007/s00603-025-04742-y.

Zou, Y., Li, S., Ma, X., et al., 2018. Effects of CO_2-brine-rock interaction on porosity/permeability and mechanical properties during supercritical-CO_2 fracturing in shale reservoirs. J. Nat. Gas Sci. Eng. 49, 157–168. https://doi.org/10.1016/j.jngse.2017.11.004.